

Node-based uniform strain virtual elements for compressible and nearly incompressible plane elasticity

A. Ortiz-Bernardin^{a,*}, R. Silva-Valenzuela^a, S. Salinas^b, N. Hitschfeld-Kahler^b, S. Luza^a, B. Rebolledo^a

^a*Computational and Applied Mechanics Laboratory, Department of Mechanical Engineering, Universidad de Chile, Av. Beauchef 851, Santiago 8370456, Chile.*

^b*Department of Computer Science, Universidad de Chile, Av. Beauchef 851, Santiago 8370456, Chile.*

Abstract

We propose a displacement-based approach to solve problems in compressible and nearly incompressible plane elasticity that combines a nodal integration technique and the virtual element method (VEM), wherein the strain is averaged around nodes from the strain of surrounding virtual elements. For the strain averaging procedure, a nodal averaging operator is constructed using a generalization to virtual elements of the node-based uniform strain approach for finite elements. We refer to these new elements as node-based uniform strain virtual elements (NVEM). A salient feature of the NVEM is that the stresses and strains become nodal variables just like displacements, which can be exploited in nonlinear simulations thereby providing room for further development of this novel approach. Through several benchmark problems in plane elasticity, we demonstrate that the NVEM is accurate and optimally convergent, and devoid of volumetric locking in the nearly incompressible limit.

Keywords: Virtual element method, Nodal integration, Strain averaging, Uniform strain, Linear elasticity, Volumetric locking

1. Introduction

We propose a displacement-based approach to solve problems in compressible and nearly incompressible plane elasticity that combines a nodal integration technique and the virtual element

*Corresponding author. Tel: +56 2 2978 4664, Fax: +56 2 2689 6057,
Email address: aortizb@uchile.cl (A. Ortiz-Bernardin)

method (VEM), wherein the strain is averaged around nodes from the strain of surrounding virtual elements. The proposed method differs from existing virtual element methods for compressible and nearly incompressible elasticity in the following aspects:

- In the proposed approach, the volumetric locking is alleviated by the averaging of the strains at the nodes and the stabilization matrix chosen. No additional degrees of freedom are introduced (displacement-based formulation). In the existing VEM approaches, the volumetric locking is alleviated by the B-bar formulation [1, 2], mixed formulation [3], enhanced strain formulation [4], hybrid formulation [5], nonconforming formulations [6–8], or addition of degrees of freedom related to the normal components of the displacement field on the element’s edges to satisfy the inf-sup condition [9].
- The strains and stresses in the proposed approach are projected to the nodes thus becoming nodal quantities just like displacements, whereas in the existing approaches these are projected inside the elements thus becoming element quantities.

Nodal integration dates from the work of Beissel and Belytschko [10] for meshfree Galerkin methods, where nodal integration emerged as an alternative to Gauss integration to accelerate the numerical integration of the weak form integrals. The fundamental difference between these two type of integration is that in nodal integration the weak form integrals are sampled at the nodes, whereas in Gauss integration the integrals are numerically integrated in the interior of the elements using cubature. Thus, in nodal integration the state and history-dependent variables in the weak form integrals naturally become nodal quantities, whereas in Gauss integration these variables become element quantities. The obvious advantages of nodal integration over Gauss integration can be summarized as follows. There are much less nodes than Gauss points in the mesh, which results in huge computational savings when nodal integration is employed. In nonlinear computations, the state and history-dependent variables are tracked only at the nodes. This feature can be exploited to avoid remapping algorithms (see, for instance, [11]) that are required in traditional Lagrangian finite element large deformation simulations with remeshing [12–15].

After the work of Beissel and Belytschko [10] nodal integration attracted great interest from the meshfree community (e.g., see Refs. [16–26]) due to the improved robustness of this type of

integration over cell-based Gauss integration. Even though nodal integration greatly improves the computational cost of meshfree Galerkin simulations, still there exists the computational burden of meshfree basis functions (e. g., moving least-squares [27, 28], reproducing kernel [29] and maximum-entropy [30–32] approximants), which includes the solution of an optimization problem and a neighbor search at every integration node. In addition, some meshfree approximations are noninterpolatory, which complicates the imposition of Dirichlet boundary conditions (additional procedures are required). Regarding finite elements, until today there are various approaches using nodal integration in which some form of pressure or strain averaging around nodes is employed. This is the case of the average nodal pressure tetrahedral element [33], the node-based uniform strain triangular and tetrahedral elements [34], the averaged nodal deformation gradient linear tetrahedral element [35], and the family of nodally integrated continuum elements (NICE) and its derivative approaches [36–39, 39–42]. Recently, the node-based uniform strain approach [34] was adopted in the nodal particle finite element method (N-PFEM) [43, 44].

Nodal integration is prone to instabilities and thus it requires stabilization. A summary of the stability issue in nodal integration is provided in Ref. [11], where also a gradient-based stabilization is proposed for small and Lagrangian large deformation simulations. Stabilization in nodal integration results in a decomposition of the stiffness matrix into a consistency part and a stability part like in the virtual element method.

The virtual element approximation is interpolatory and, being a generalization of finite elements, does not have the computational burden of meshfree methods. Its computational cost is comparable to that of the finite element method [45]. In addition, it is equipped with a stabilization procedure like in nodal integration. Regarding its sensitivity to mesh distortions, several authors have reported very robust solutions under mesh distortions [1, 46–50] and highly nonconvex elements [2, 51–53]. Therefore, it is our opinion that the VEM will play a key role in the development of efficient and robust nodal integration techniques especially in extreme large deformations.

In this exploratory paper, a nodal integration scheme for virtual elements is proposed using ideas taken from the node-based uniform strain approach of Dohrmann et al. [34] for finite elements, wherein the strain is averaged around nodes from the strain of surrounding elements. We refer to

these new elements as node-based uniform strain virtual elements (NVEM). The focus in this paper is on plane elasticity, whose governing equations are provided in Section 2. Section 3 summarizes the theoretical framework of the VEM for plane elasticity. Node-based uniform strain virtual elements are developed in Section 4. Stabilizations for the NVEM are discussed in Section 5. The numerical behavior of the NVEM is examined through several benchmark problems in compressible and nearly incompressible elasticity in Section 6. Some concluding remarks along with ongoing and future research directions are discussed in Section 7.

2. Governing equations

Consider an elastic body that occupies the open domain $\Omega \subset \mathbb{R}^2$ and is bounded by the one-dimensional surface Γ whose unit outward normal is \mathbf{n}_Γ . The boundary is assumed to admit decompositions $\Gamma = \Gamma_D \cup \Gamma_N$ and $\emptyset = \Gamma_D \cap \Gamma_N$, where Γ_D is the Dirichlet boundary and Γ_N is the Neumann boundary. The closure of the domain is $\overline{\Omega} = \Omega \cup \Gamma$. Let $\mathbf{u}(\mathbf{x}) : \overline{\Omega} \rightarrow \mathbb{R}^2$ be the displacement field at a point \mathbf{x} of the elastic body when the body is subjected to external tractions $\mathbf{t}_N(\mathbf{x}) : \Gamma_N \rightarrow \mathbb{R}^2$ and body forces $\mathbf{b}(\mathbf{x}) : \Omega \rightarrow \mathbb{R}^2$. The imposed Dirichlet (essential) boundary conditions are $\mathbf{u}_D(\mathbf{x}) : \Gamma_D \rightarrow \mathbb{R}^2$. The boundary-value problem for linear elastostatics is: find $\mathbf{u}(\mathbf{x}) : \overline{\Omega} \rightarrow \mathbb{R}^2$ such that

$$\nabla \cdot \boldsymbol{\sigma} + \mathbf{b} = 0 \quad \text{in } \Omega, \quad (1a)$$

$$\mathbf{u} = \mathbf{u}_D \quad \text{on } \Gamma_D, \quad (1b)$$

$$\boldsymbol{\sigma} \cdot \mathbf{n}_\Gamma = \mathbf{t}_N \quad \text{on } \Gamma_N, \quad (1c)$$

where $\boldsymbol{\sigma}$ is the Cauchy stress tensor.

The Galerkin weak formulation of the above problem reads: find $\mathbf{u}(\mathbf{x}) \in \mathcal{V}$ such that

$$\begin{aligned} a(\mathbf{u}, \mathbf{v}) &= \ell(\mathbf{v}) \quad \forall \mathbf{v}(\mathbf{x}) \in \mathcal{W}, \\ a(\mathbf{u}, \mathbf{v}) &= \int_{\Omega} \boldsymbol{\sigma}(\mathbf{u}) : \boldsymbol{\varepsilon}(\mathbf{v}) \, d\mathbf{x}, \quad \ell(\mathbf{v}) = \int_{\Omega} \mathbf{b} \cdot \mathbf{v} \, d\mathbf{x} + \int_{\Gamma_N} \mathbf{t}_N \cdot \mathbf{v} \, ds, \end{aligned} \quad (2)$$

where \mathcal{V} denotes the space of admissible displacements and \mathcal{W} the space of its variations, and $\boldsymbol{\varepsilon}$ is

the small strain tensor that is given by

$$\boldsymbol{\varepsilon}(\mathbf{u}) = \frac{1}{2} (\mathbf{u} \otimes \boldsymbol{\nabla} + \boldsymbol{\nabla} \otimes \mathbf{u}). \quad (3)$$

3. Virtual element method for plane elasticity

The virtual element method (VEM) [54] is a generalization of the finite element method (FEM) that can deal with very general meshes formed by elements with arbitrary number of edges (convex or non-convex polygons), and the mesh can even include elements with coplanar edges and collapsing nodes, and non-matching elements. In the VEM, the displacement field is decomposed into a polynomial part and other terms by using a projection operator. Altogether, this procedure ends up with no explicit computation of basis functions (basis functions are *virtual*), and an algebraic construction of the element stiffness matrix is realized. The virtual element stiffness matrix results in the following decomposition:

$$\mathbf{K}_E = \mathbf{K}_E^c + \mathbf{K}_E^s, \quad (4)$$

where \mathbf{K}_E^c is the consistency part of the element stiffness matrix, which provides consistency to the method (i.e., ensures patch test satisfaction), and \mathbf{K}_E^s is the stability part of the element stiffness matrix, which provides stability.

A brief summary of the VEM for plane elasticity is given next. All the derivations are presented at the element level. Concerning the element, the following notation is used: the element is denoted by E and its boundary by ∂E . The area of the element is denoted by $|E|$. The number of edges and nodes of an element are denoted by N_E^V . The unit outward normal to the element boundary in the Cartesian coordinate system is denoted by $\mathbf{n} = [n_1 \ n_2]^T$. Fig. 1 depicts an element with five edges ($N_E^V = 5$), where the edge e_a of length $|e_a|$ and the edge e_{a-1} of length $|e_{a-1}|$ are the element edges incident to node a , and \mathbf{n}_a and \mathbf{n}_{a-1} are the unit outward normals to these edges, respectively.

3.1. Projection operator

The VEM essentially relies upon the decomposition of the displacement field into its polynomial part and some additional terms that, in general, are nonpolynomials. To this end, a projection

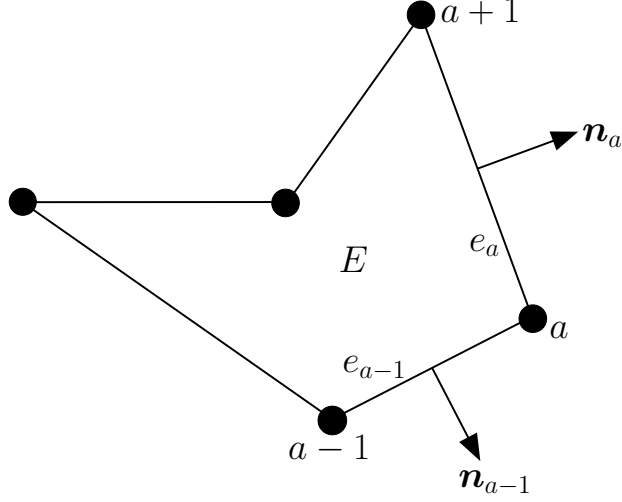


Fig. 1: Schematic representation of a polygonal element of $N_E^V = 5$ edges.

operator Π is defined such that

$$\mathbf{u}_h = \Pi \mathbf{u}_h + (\mathbf{u}_h - \Pi \mathbf{u}_h), \quad (5)$$

where $\Pi \mathbf{u}_h$ contains the polynomial terms and $\mathbf{u}_h - \Pi \mathbf{u}_h$ the nonpolynomial terms.

In this paper, we restrict ourselves to low-order approximations, that is Π is meant to project onto the space of linear polynomials. At the element level, this projection operator onto the linear displacements can be defined as [25, 45, 55, 56]:

$$\Pi \mathbf{u}_h = \begin{bmatrix} (x_1 - \bar{x}_1) & 0 & \frac{1}{2}(x_2 - \bar{x}_2) & 1 & 0 & \frac{1}{2}(x_2 - \bar{x}_2) \\ 0 & (x_2 - \bar{x}_2) & \frac{1}{2}(x_1 - \bar{x}_1) & 0 & 1 & -\frac{1}{2}(x_1 - \bar{x}_1) \end{bmatrix} \begin{bmatrix} \hat{\varepsilon}_{11} \\ \hat{\varepsilon}_{22} \\ 2\hat{\varepsilon}_{12} \\ \bar{u}_{1h} \\ \bar{u}_{2h} \\ 2\hat{\omega}_{12} \end{bmatrix}, \quad (6)$$

where \bar{x}_1 and \bar{x}_2 are the components of the mean value of the nodal coordinates of the element,

$$\bar{\mathbf{x}} = \begin{bmatrix} \bar{x}_1 \\ \bar{x}_2 \end{bmatrix} = \frac{1}{N_E^V} \sum_{a=1}^{N_E^V} \mathbf{x}(\mathbf{x}_a) = \frac{1}{N_E^V} \sum_{a=1}^{N_E^V} \mathbf{x}_a, \quad (7)$$

and \bar{u}_{1h} and \bar{u}_{2h} are the components of the mean value of the nodal element displacements,

$$\bar{\mathbf{u}} = \begin{bmatrix} \bar{u}_{1h} \\ \bar{u}_{2h} \end{bmatrix} = \frac{1}{N_E^V} \sum_{a=1}^{N_E^V} \mathbf{u}_h(\mathbf{x}_a). \quad (8)$$

The terms $\hat{\varepsilon}_{ij}$ are components of the element average $\hat{\varepsilon} = \frac{1}{|E|} \int_E \boldsymbol{\varepsilon} d\mathbf{x}$, and $\hat{\omega}_{12}$ is the component of the element average $\hat{\omega} = \frac{1}{|E|} \int_E \boldsymbol{\omega} d\mathbf{x}$, where $\boldsymbol{\omega}$ is the skew-symmetric tensor that represents rotations. These element averages are evaluated on the boundary of E by invoking the divergence theorem, which gives the following identities:

$$\hat{\varepsilon}(\mathbf{u}_h) = \frac{1}{|E|} \int_E \boldsymbol{\varepsilon}(\mathbf{u}_h) d\mathbf{x} = \frac{1}{2|E|} \int_{\partial E} (\mathbf{u}_h \otimes \mathbf{n} + \mathbf{n} \otimes \mathbf{u}_h) ds, \quad (9)$$

$$\hat{\omega}(\mathbf{u}_h) = \frac{1}{|E|} \int_E \boldsymbol{\omega}(\mathbf{u}_h) d\mathbf{x} = \frac{1}{2|E|} \int_{\partial E} (\mathbf{u}_h \otimes \mathbf{n} - \mathbf{n} \otimes \mathbf{u}_h) ds. \quad (10)$$

The field variable is assumed to be discretized as

$$\mathbf{u}_h = \begin{bmatrix} u_{1h} \\ u_{2h} \end{bmatrix} = \sum_{a=1}^{N_E^V} \phi_a(\mathbf{x}) \mathbf{u}_a, \quad (11)$$

where $\{\phi_a(\mathbf{x})\}_{a=1}^{N_E^V}$ are basis functions that form a partition of unity. Eqs. (8)–(10) reveal that all what is needed regarding the basis functions is the knowledge of their behavior on the element boundary. The VEM assumes the following behavior for the basis functions on the element boundary:

- basis functions are piecewise linear (edge by edge);
- basis functions are continuous on the element edges.

In other words, the basis functions possess the Kronecker-delta property on the element edges and thus they behave like the one-dimensional hat function. It is stressed that an explicit formula for the basis functions is not needed in the VEM. Moreover, in the interior of the element the basis functions are not known. With these particular assumptions for the basis functions, the mean element nodal displacements (8), and the element averages (9) and (10), can be computed in terms of the element degrees of freedom.

3.2. VEM bilinear form

The projection operator (6) is derived¹ from the following orthogonality condition at the element level:

$$a_E(\mathbf{u}_h - \Pi \mathbf{u}_h, \mathbf{p}) = a_E(\mathbf{p}, \mathbf{v}_h - \Pi \mathbf{v}_h) = 0 \quad \forall \mathbf{p} \in [\mathcal{P}(E)]^2, \quad (12)$$

where $[\mathcal{P}(E)]^2$ is the space of linear displacements over the element. This orthogonality condition states that the nonpolynomial terms $\mathbf{u}_h - \Pi \mathbf{u}_h$ in E , measured in the energy norm, are orthogonal to $[\mathcal{P}(E)]^2$. Using the decomposition (5) along with condition (12), and noting that $\Pi \mathbf{u}_h$ and $\Pi \mathbf{v}_h \in [\mathcal{P}(E)]^2$, the following VEM representation of the bilinear form is obtained:

$$a_E(\mathbf{u}_h, \mathbf{v}_h) = a_E(\Pi \mathbf{u}_h, \Pi \mathbf{v}_h) + a_E(\mathbf{u}_h - \Pi \mathbf{u}_h, \mathbf{v}_h - \Pi \mathbf{v}_h). \quad (13)$$

The VEM bilinear form can be further elaborated. For convenience, the projection operator (6) is rewritten as

$$\Pi \mathbf{u}_h = \mathbf{h}(\mathbf{x}) \widehat{\boldsymbol{\varepsilon}}(\mathbf{u}_h) + \mathbf{g}(\mathbf{x}) \mathbf{r}(\mathbf{u}_h), \quad (14)$$

where

$$\mathbf{h}(\mathbf{x}) = \begin{bmatrix} (x_1 - \bar{x}_1) & 0 & \frac{1}{2}(x_2 - \bar{x}_2) \\ 0 & (x_2 - \bar{x}_2) & \frac{1}{2}(x_1 - \bar{x}_1) \end{bmatrix}, \quad \mathbf{g}(\mathbf{x}) = \begin{bmatrix} 1 & 0 & \frac{1}{2}(x_2 - \bar{x}_2) \\ 0 & 1 & -\frac{1}{2}(x_1 - \bar{x}_1) \end{bmatrix}, \quad (15)$$

$$\mathbf{r}(\mathbf{u}_h) = \begin{bmatrix} \bar{u}_{1h} & \bar{u}_{2h} & 2\widehat{\omega}_{12} \end{bmatrix}^\top, \quad (16)$$

¹The derivation is given in Ref. [25]

and

$$\widehat{\boldsymbol{\varepsilon}}(\mathbf{u}_h) = \begin{bmatrix} \widehat{\varepsilon}_{11} & \widehat{\varepsilon}_{22} & 2\widehat{\varepsilon}_{12} \end{bmatrix}^\top \quad (17)$$

is the vector form of the element average strain. From now on, we always use this vector form when referring to the element average strain $\widehat{\boldsymbol{\varepsilon}}$.

Using the bilinear form written in terms of the vector form of the strain, that is, $a(\mathbf{u}_h, \mathbf{v}_h) = \int_\Omega \boldsymbol{\varepsilon}^\top(\mathbf{v}_h) \mathbf{D} \boldsymbol{\varepsilon}(\mathbf{u}_h)$, where \mathbf{D} is the constitutive matrix, and noting that $\mathbf{r}(\mathbf{u}_h)$ represents rigid body translations and rotation, and that these do not produce strain energy, the first term on the right-hand side of (13) can be written, as follows:

$$\begin{aligned} a_E(\Pi \mathbf{u}_h, \Pi \mathbf{v}_h) &= \int_E \begin{bmatrix} \frac{\partial \Pi v_{1h}}{\partial x_1} & \frac{\partial \Pi v_{2h}}{\partial x_2} & \frac{\partial \Pi v_{1h}}{\partial x_2} + \frac{\partial \Pi v_{2h}}{\partial x_1} \end{bmatrix} \mathbf{D} \begin{bmatrix} \frac{\partial \Pi u_{1h}}{\partial x_1} \\ \frac{\partial \Pi u_{2h}}{\partial x_2} \\ \frac{\partial \Pi u_{1h}}{\partial x_2} + \frac{\partial \Pi u_{2h}}{\partial x_1} \end{bmatrix} d\mathbf{x} \\ &= \int_E \widehat{\boldsymbol{\varepsilon}}^\top(\mathbf{v}_h) \mathbf{D} \widehat{\boldsymbol{\varepsilon}}(\mathbf{u}_h) d\mathbf{x}. \end{aligned} \quad (18)$$

For an isotropic linear elastic material, the constitutive matrix is given by

$$\mathbf{D} = \frac{E_Y}{(1+\nu)(1-2\nu)} \begin{bmatrix} 1-\nu & \nu & 0 \\ \nu & 1-\nu & 0 \\ 0 & 0 & \frac{1-2\nu}{2} \end{bmatrix} \quad (19)$$

for plane strain condition, and

$$\mathbf{D} = \frac{E_Y}{1-\nu^2} \begin{bmatrix} 1 & \nu & 0 \\ \nu & 1 & 0 \\ 0 & 0 & \frac{1-\nu}{2} \end{bmatrix} \quad (20)$$

for plane stress condition, where E_Y is the Young's modulus and ν is the Poisson's ratio.

The second term on the right-hand side of (13) can be written as

$$a_E(\mathbf{u}_h - \Pi \mathbf{u}_h, \mathbf{v}_h - \Pi \mathbf{v}_h) = (\mathbf{1} - \Pi)^\top a_E(\mathbf{v}_h, \mathbf{u}_h) (\mathbf{1} - \Pi), \quad (21)$$

which reveals that $a_E(\mathbf{u}_h - \Pi \mathbf{u}_h, \mathbf{v}_h - \Pi \mathbf{v}_h)$ is not computable as $a_E(\mathbf{v}_h, \mathbf{u}_h)$ would need to be evaluated inside the element using quadrature, but the VEM basis functions are not known inside the element. However, since $a_E(\mathbf{u}_h - \Pi \mathbf{u}_h, \mathbf{v}_h - \Pi \mathbf{v}_h)$ is meant to only provide stability, $a_E(\mathbf{v}_h, \mathbf{u}_h)$ can be conveniently approximated by a bilinear form $s_E(\cdot, \cdot)$ that is computable while preserving the coercivity of the system. In other words, $s_E(\mathbf{v}_h, \mathbf{u}_h)$ must be positive definite and scale like $a_E(\cdot, \cdot)$ in the kernel of Π [54, 55].

Using (18) and (21) with the approximation $a_E(\mathbf{v}_h, \mathbf{u}_h) = s_E(\mathbf{v}_h, \mathbf{u}_h)$, the VEM bilinear form for plane elasticity is written as

$$a_{h,E}(\mathbf{u}_h, \mathbf{v}_h) = \int_E \hat{\boldsymbol{\varepsilon}}^\top(\mathbf{v}_h) \mathbf{D} \hat{\boldsymbol{\varepsilon}}(\mathbf{u}_h) d\mathbf{x} + (\mathbf{1} - \Pi)^\top s_E(\mathbf{v}_h, \mathbf{u}_h) (\mathbf{1} - \Pi) \quad (22)$$

3.3. VEM element stiffness matrix

The discrete element average strain is computed, as follows:

$$\hat{\boldsymbol{\varepsilon}}_h(\mathbf{u}_h) = \hat{\boldsymbol{\varepsilon}} \left(\sum_{a=1}^{N_E^V} \phi_a(\mathbf{x}) \mathbf{u}_a \right) = \mathbf{B} \mathbf{d}, \quad (23)$$

where \mathbf{d} is the vector of element degrees of freedom (or element nodal displacements), and

$$\mathbf{B} = \begin{bmatrix} \mathbf{B}_1 & \cdots & \mathbf{B}_a & \cdots & \mathbf{B}_{N_E^V} \end{bmatrix}, \quad \mathbf{B}_a = \begin{bmatrix} q_{1a} & 0 \\ 0 & q_{2a} \\ q_{2a} & q_{1a} \end{bmatrix}, \quad (24)$$

where $q_{ia} = \frac{1}{|E|} \int_{\partial E} \phi_a(\mathbf{x}) n_i ds$. Since the VEM basis functions are assumed to be piecewise linear (edge by edge) and continuous on the element boundary, q_{ia} can be exactly computed using a trapezoidal rule, which gives the following algebraic expression:

$$q_{ia} = \frac{1}{2|E|} (|e_{a-1}| n_{i(a-1)} + |e_a| n_{ia}), \quad i = 1, 2, \quad (25)$$

where n_{ia} is the i -th component of \mathbf{n}_a and $|e_a|$ is the length of the edge incident to node a as defined in Fig. 1. Therefore, since $\hat{\boldsymbol{\varepsilon}}$ and \mathbf{D} are constant over the element, the discrete version of

the first term on the right-hand side of (22) is written as

$$\int_E \widehat{\boldsymbol{\varepsilon}}_h^\top(\mathbf{v}_h) \mathbf{D} \widehat{\boldsymbol{\varepsilon}}_h(\mathbf{u}_h) d\mathbf{x} = |E| \widehat{\boldsymbol{\varepsilon}}_h^\top(\mathbf{v}_h) \mathbf{D} \widehat{\boldsymbol{\varepsilon}}_h(\mathbf{u}_h) = \mathbf{q}^\top \left(|E| \mathbf{B}^\top \mathbf{D} \mathbf{B} \right) \mathbf{d}, \quad (26)$$

where \mathbf{q} is the vector of nodal variations.

To build a computable version of (21), the discretization of Π is required. This demands the discretization of $h(\mathbf{x})$, $\widehat{\boldsymbol{\varepsilon}}(\mathbf{u}_h)$, $g(\mathbf{x})$ and $r(\mathbf{u}_h)$. The discretization of $\widehat{\boldsymbol{\varepsilon}}(\mathbf{u}_h)$ is given in (23). The remainder terms are discretized, as follows:

$$\mathbf{h}_h(\mathbf{x}) = \sum_{a=1}^{N_E^V} \phi_a(\mathbf{x}) \mathbf{h}(\mathbf{x}_a) = \mathbf{N} \mathbf{H}, \quad (27)$$

$$\mathbf{g}_h(\mathbf{x}) = \sum_{a=1}^{N_E^V} \phi_a(\mathbf{x}) \mathbf{g}(\mathbf{x}_a) = \mathbf{N} \mathbf{G}, \quad (28)$$

$$\mathbf{r}_h = \mathbf{r} \left(\sum_{a=1}^{N_E^V} \phi_a(\mathbf{x}) \mathbf{u}_a \right) = \mathbf{R} \mathbf{d}, \quad (29)$$

where

$$\mathbf{N} = \begin{bmatrix} \mathbf{N}_1 & \cdots & \mathbf{N}_a & \cdots & \mathbf{N}_{N_E^V} \end{bmatrix}, \quad \mathbf{N}_a = \begin{bmatrix} \phi_a(\mathbf{x}) & 0 \\ 0 & \phi_a(\mathbf{x}) \end{bmatrix}, \quad (30)$$

$$\mathbf{H} = \begin{bmatrix} \mathbf{H}_1 \\ \vdots \\ \mathbf{H}_a \\ \vdots \\ \mathbf{H}_{N_E^V} \end{bmatrix}, \quad \mathbf{H}_a = \begin{bmatrix} (x_{1a} - \bar{x}_1) & 0 & \frac{1}{2}(x_{2a} - \bar{x}_2) \\ 0 & (x_{2a} - \bar{x}_2) & \frac{1}{2}(x_{1a} - \bar{x}_1) \end{bmatrix}, \quad (31)$$

$$\mathbf{G} = \begin{bmatrix} \mathbf{G}_1 \\ \vdots \\ \mathbf{G}_a \\ \vdots \\ \mathbf{G}_{N_E^V} \end{bmatrix}, \quad \mathbf{G}_a = \begin{bmatrix} 1 & 0 & \frac{1}{2}(x_{2a} - \bar{x}_2) \\ 0 & 1 & -\frac{1}{2}(x_{1a} - \bar{x}_1) \end{bmatrix}, \quad (32)$$

and

$$\mathbf{R} = \begin{bmatrix} \mathbf{R}_1 & \cdots & \mathbf{R}_a & \cdots & \mathbf{R}_{N_E^V} \end{bmatrix}, \quad \mathbf{R}_a = \begin{bmatrix} \frac{1}{N_E^V} & 0 \\ 0 & \frac{1}{N_E^V} \\ q_{2a} & -q_{1a} \end{bmatrix}. \quad (33)$$

Therefore, the discrete Π can be written as

$$\Pi_h \mathbf{u}_h = \mathbf{NHBd} + \mathbf{NGRd} = \mathbf{N}(\mathbf{HB} + \mathbf{GR})\mathbf{d}, \quad (34)$$

which defines the projection matrix as

$$\mathbf{P} = \mathbf{HB} + \mathbf{GR}. \quad (35)$$

Using the projection matrix and the discrete field $\mathbf{u}_h = \sum_{a=1}^{N_E^V} \phi_a(\mathbf{x})\mathbf{u}_a = \mathbf{Nd}$, the discrete version of the second term on the right-hand side of (22) is

$$\mathbf{q}^\top (\mathbf{I} - \mathbf{P})^\top s_E(\mathbf{N}^\top, \mathbf{N})(\mathbf{I} - \mathbf{P})\mathbf{d} = \mathbf{q}^\top (\mathbf{I} - \mathbf{P})^\top \mathbf{S}(\mathbf{I} - \mathbf{P})\mathbf{d}. \quad (36)$$

Finally, using (26) and (36) the discrete VEM bilinear form is written as

$$a_{h,E}(\mathbf{u}_h, \mathbf{v}_h) = \mathbf{q}^\top \left\{ |E| \mathbf{B}^\top \mathbf{D} \mathbf{B} + (\mathbf{I} - \mathbf{P})^\top \mathbf{S}(\mathbf{I} - \mathbf{P}) \right\} \mathbf{d}, \quad (37)$$

which defines the element stiffness matrix as the sum of the element consistency stiffness matrix,

\mathbf{K}_E^c , and the element stability stiffness matrix, \mathbf{K}_E^s , as follows:

$$\mathbf{K}_E = \mathbf{K}_E^c + \mathbf{K}_E^s, \quad \mathbf{K}_E^c = |E| \mathbf{B}^\top \mathbf{D} \mathbf{B}, \quad \mathbf{K}_E^s = (\mathbf{I} - \mathbf{P})^\top \mathbf{S} (\mathbf{I} - \mathbf{P}). \quad (38)$$

3.4. VEM element force vector

For linear fields, the VEM version of the loading term in the weak form (2) is computed at the element level, as follows [46, 54, 57]:

$$\ell_E^b(\mathbf{v}_h) = \int_E \widehat{\mathbf{b}} \cdot \bar{\mathbf{v}}_h \, d\mathbf{x} = |E| \widehat{\mathbf{b}} \cdot \bar{\mathbf{v}}_h, \quad \widehat{\mathbf{b}} = \frac{1}{|E|} \int_E \mathbf{b} \, d\mathbf{x} \quad (39)$$

for the loading term associated with the body forces, and similarly

$$\ell_e^t(\mathbf{v}_h) = |e| \widehat{\mathbf{t}}_N \cdot \bar{\mathbf{v}}_h, \quad \widehat{\mathbf{t}}_N = \frac{1}{|e|} \int_e \mathbf{t}_N \, ds \quad (40)$$

for the loading term associated with the tractions on the Neumann boundary, where e and $|e|$ are as defined in Fig. 1 for an element's edge located on the Neumann boundary. The discrete versions of these loading terms are $\ell_{h,E}^b(\mathbf{v}_h) = \mathbf{q}^\top \mathbf{f}_E^b$ and $\ell_{h,e}^t(\mathbf{v}_h) = \mathbf{q}^\top \mathbf{f}_e^t$, where \mathbf{f}_E^b and \mathbf{f}_e^t are the element force vectors given, respectively, by

$$\mathbf{f}_E^b = |E| \bar{\mathbf{N}}^\top \widehat{\mathbf{b}}, \quad (41)$$

where

$$\bar{\mathbf{N}} = \begin{bmatrix} \bar{\mathbf{N}}_1 & \cdots & \bar{\mathbf{N}}_a & \cdots & \bar{\mathbf{N}}_{N_E^V} \end{bmatrix}, \quad \bar{\mathbf{N}}_a = \begin{bmatrix} \frac{1}{N_E^V} & 0 \\ 0 & \frac{1}{N_E^V} \end{bmatrix}, \quad (42)$$

and

$$\mathbf{f}_e^t = |e| \bar{\mathbf{N}}_\Gamma^\top \widehat{\mathbf{t}}_N, \quad (43)$$

where

$$\bar{\mathbf{N}}_\Gamma = \begin{bmatrix} \frac{1}{N_e^V} & 0 & \frac{1}{N_e^V} & 0 \\ 0 & \frac{1}{N_e^V} & 0 & \frac{1}{N_e^V} \end{bmatrix} = \begin{bmatrix} \frac{1}{2} & 0 & \frac{1}{2} & 0 \\ 0 & \frac{1}{2} & 0 & \frac{1}{2} \end{bmatrix} \quad (44)$$

since the number of vertices of an edge is $N_e^V = 2$.

4. Node-based uniform strain virtual elements

The virtual element method for plane elasticity described in Section 3 is prone to volumetric locking in the limit $\nu \rightarrow 0.5$. We propose to use a nodal averaging operator π_I in (13) that is designed to preclude volumetric locking without introducing additional degrees of freedom. This nodal averaging operator leads to a nodal version of the VEM bilinear form, as follows:

$$a_{h,I}(\mathbf{u}_h, \mathbf{v}_h) = a_I(\pi_I[\Pi \mathbf{u}_h], \pi_I[\Pi \mathbf{v}_h]) + s_I(\pi_I[\mathbf{u}_h - \Pi \mathbf{u}_h], \pi_I[\mathbf{v}_h - \Pi \mathbf{v}_h]), \quad (45)$$

where according to the VEM theory, $s_I(\pi_I[\mathbf{u}_h - \Pi \mathbf{u}_h], \pi_I[\mathbf{v}_h - \Pi \mathbf{v}_h])$ is a computable approximation to $a_I(\pi_I[\mathbf{u}_h - \Pi \mathbf{u}_h], \pi_I[\mathbf{v}_h - \Pi \mathbf{v}_h])$ and is meant to provide stability.

4.1. Construction of the nodal averaging operator

The central idea is to associate a patch of virtual elements with each node of the mesh. The patch for node I is denoted by \mathcal{T}_I and is defined as the set of virtual elements connected to node I (see Fig. 2). Each node of a virtual element E in the patch is assigned the area $\frac{1}{N_E^V}|E|$, that is, the area of an element is uniformly distributed among its nodes. The representative area of node I is denoted by $|I|$ and is computed by addition of all the areas that are assigned to node I from the elements in \mathcal{T}_I , that is,

$$|I| = \sum_{E \in \mathcal{T}_I} \frac{1}{N_E^V} |E|. \quad (46)$$

Similarly, each node of a virtual element E is uniformly assigned the strain $\frac{1}{N_E^V} \widehat{\boldsymbol{\varepsilon}}(\mathbf{u}_h)$. The *node-based uniform strain* is computed by nodal averaging around node I , as follows:

$$\boldsymbol{\varepsilon}_I(\mathbf{u}_h) = \frac{1}{|I|} \sum_{E \in \mathcal{T}_I} |E| \frac{1}{N_E^V} \widehat{\boldsymbol{\varepsilon}}(\mathbf{u}_h). \quad (47)$$

Since $\widehat{\boldsymbol{\varepsilon}}(\mathbf{u}_h)$ is by definition given at the element level, then from Eq. (47) the following nodal averaging operator is proposed:

$$\pi_I[\cdot] = \frac{1}{|I|} \sum_{E \in \mathcal{T}_I} |E| \frac{1}{N_E^V} [\cdot]_E, \quad (48)$$

where $[\cdot]_E$ denotes evaluation over the element E . Using this nodal averaging operator, the nodal representation of a function F , which can be a scalar, a vector, a matrix or a tensor, is obtained as

$$F_I = \pi_I[F] = \frac{1}{|I|} \sum_{E \in \mathcal{T}_I} |E| \frac{1}{N_E^V} [F]_E. \quad (49)$$

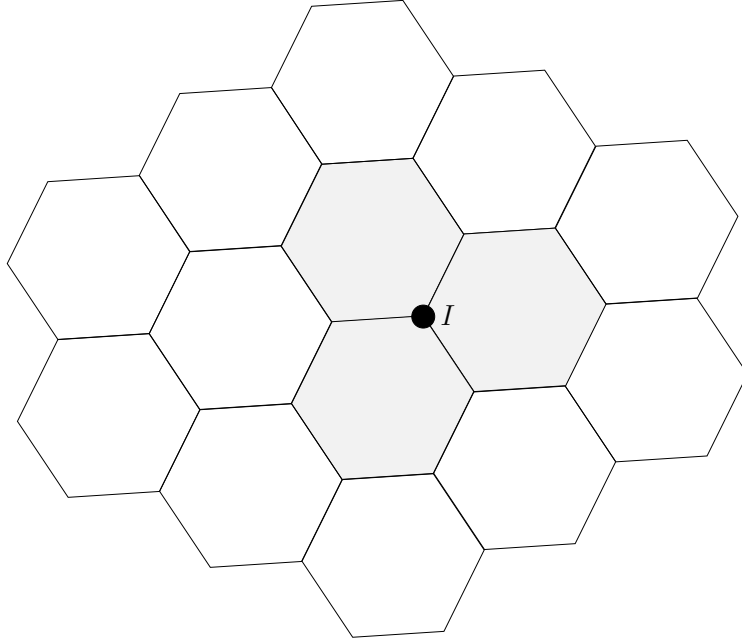


Fig. 2: Nodal patch \mathcal{T}_I (shaded elements) formed by the virtual elements connected to node I .

The idea of having a nodal strain that is representative of the patch \mathcal{T}_I (like the one defined in (47)) has long been used in meshfree and finite element nodal integration techniques [11, 21, 33–37, 39, 40, 58]. In particular, the node-based uniform strain approach was developed for three-node triangular and four-node tetrahedral elements in Ref. [34], and proved to perform well for nearly incompressible solids. However, that approach presented instability issues in some particular cases and required stabilization [11]. Within the VEM framework stabilization is obtained by construction of the method, and thus in combining the node-based uniform strain approach with the VEM framework no instability issues arise.

4.2. Nodal VEM bilinear form

Using the nodal averaging operator (48), the nodal representation of the VEM bilinear form for plane elasticity (Eq. (22)) is written as

$$a_{h,I}(\mathbf{u}_h, \mathbf{v}_h) = |I| \boldsymbol{\varepsilon}_I^\top(\mathbf{v}_h) \mathbf{D} \boldsymbol{\varepsilon}_I(\mathbf{u}_h) + (\mathbf{1} - \Pi)_I^\top s_I(\mathbf{v}_h, \mathbf{u}_h) (\mathbf{1} - \Pi)_I. \quad (50)$$

Letting N be the total number of nodes in the mesh, the global bilinear form is obtained by summing through all of them, as follows:

$$a_h(\mathbf{u}_h, \mathbf{v}_h) = \sum_{I=1}^N \left[|I| \boldsymbol{\varepsilon}_I^\top(\mathbf{v}_h) \mathbf{D} \boldsymbol{\varepsilon}_I(\mathbf{u}_h) + (\mathbf{1} - \Pi)_I^\top s_I(\mathbf{v}_h, \mathbf{u}_h) (\mathbf{1} - \Pi)_I \right]. \quad (51)$$

4.3. Nodal VEM element stiffness matrix

The nodal VEM element stiffness matrix that arises from (50) is the nodal version of (38). This gives

$$\mathbf{K}_I = \mathbf{K}_I^c + \mathbf{K}_I^s, \quad \mathbf{K}_I^c = |I| \mathbf{B}_I^\top \mathbf{D} \mathbf{B}_I, \quad \mathbf{K}_I^s = (\mathbf{I} - \mathbf{P})_I^\top \mathbf{S}_I (\mathbf{I} - \mathbf{P})_I, \quad (52)$$

where $\mathbf{B}_I = \pi_I[\mathbf{B}]$, $(\mathbf{I} - \mathbf{P})_I = \pi_I[\mathbf{I} - \mathbf{P}]$, and \mathbf{S}_I is defined in Section 5.

4.4. Nodal VEM element force vector

The nodal VEM element force vector associated with the body forces is the nodal representation of (41) and is given by

$$\mathbf{f}_I^b = |I| \bar{\mathbf{N}}_I^\top \hat{\mathbf{b}}_I, \quad (53)$$

where $\bar{\mathbf{N}}_I = \pi_I[\bar{\mathbf{N}}]$ and $\hat{\mathbf{b}}_I = \pi_I[\hat{\mathbf{b}}]$. Similarly, the nodal VEM element force vector associated with the tractions is given by the nodal representation of (43), as follows:

$$\mathbf{f}_I^t = |I| \bar{\mathbf{N}}_{\Gamma,I}^\top \hat{\mathbf{t}}_{N,I}, \quad (54)$$

where the nodal components are now computed with respect to the one-dimensional domain on the Neumann boundary, that is, $|I| = \sum_{e \in \mathcal{T}_I} \frac{1}{2}|e|$, where e is an element's edge located on the

Neumann boundary and $|e|$ its length; \mathcal{T}_I now represents the set of edges connected to node I on the Neumann boundary. Proceeding as mentioned, the remainder nodal matrices are

$$\bar{\mathbf{N}}_{\Gamma,I} = \frac{1}{|I|} \sum_{e \in \mathcal{T}_I} |e| \frac{1}{2} [\bar{\mathbf{N}}_\Gamma]_e, \quad (55)$$

and

$$\hat{\mathbf{t}}_{N,I} = \frac{1}{|I|} \sum_{e \in \mathcal{T}_I} |e| \frac{1}{2} [\hat{\mathbf{t}}_N]_e. \quad (56)$$

5. Stabilization for node-based uniform strain virtual elements

Within the VEM framework, stabilization is one of the key ingredients to guarantee convergence. However, in nodal integration, stabilization can make the formulation somewhat stiff in the nearly incompressible limit [21]. To mitigate this, a modified constitutive matrix $\tilde{\mathbf{D}}$ can be used in lieu of the standard \mathbf{D} when computing the stability matrix. We opt for $\tilde{\mathbf{D}}$ given as follows [11]:

$$\tilde{\mathbf{D}} = \mathbf{D}(\tilde{E}, \tilde{\nu}), \quad (57)$$

where

$$\tilde{E} = \frac{\tilde{\nu} (3\tilde{\lambda} + 2\tilde{\mu})}{\tilde{\lambda} + \tilde{\mu}}, \quad \tilde{\nu} = \frac{\tilde{\lambda}}{2(\tilde{\lambda} + \tilde{\mu})}; \quad (58)$$

$\tilde{\lambda}$ and $\tilde{\mu}$ are modified Lamé's first and second parameters, respectively, and are calculated as follows:

$$\tilde{\mu} := \mu, \quad \tilde{\lambda} := \min(\lambda, 25\tilde{\mu}), \quad (59)$$

where λ and μ are the Lamé parameters of the problem to solve. Similarly, another possibility to mitigate the stiff response is the use of a modified constitutive matrix \mathbf{D}_μ given by

$$\mathbf{D}_\mu = \begin{bmatrix} 2\mu & 0 & 0 \\ 0 & 2\mu & 0 \\ 0 & 0 & \mu \end{bmatrix}. \quad (60)$$

The rationale of this approach is that when computing the stability matrix the pressure parameter $\lambda(\varepsilon_{11} + \varepsilon_{22})$, which is the responsible of the possible stiff behavior, is omitted. Alternatively, a simpler definition of \mathbf{D}_μ that produces practically identical results is obtained by using the constitutive matrix that is related to the shear deformations, i.e.,

$$\mathbf{D}_\mu = \begin{bmatrix} 0 & 0 & 0 \\ 0 & 0 & 0 \\ 0 & 0 & \mu \end{bmatrix}. \quad (61)$$

We point out that the foregoing stabilization procedure with \mathbf{D}_μ as given in (61) is similar to one of the stabilization approaches in the B-bar virtual element method [2] (see Appendix A therein).

Using the modified constitutive matrices, we define the stability matrix as the nodal version of the *D-recipe* stabilization technique [49, 59]. This gives two diagonal stability matrices whose entries are given by

$$(\mathbf{S}_I)_{i,i} = \max \left(1, (|I| \mathbf{B}_I^\top \tilde{\mathbf{D}} \mathbf{B}_I)_{i,i} \right) \quad (62)$$

and

$$(\mathbf{S}_I)_{i,i} = \max \left(1, (|I| \mathbf{B}_I^\top \mathbf{D}_\mu \mathbf{B}_I)_{i,i} \right). \quad (63)$$

We refer to (62) and (63), respectively, as $\tilde{\mathbf{D}}$ and \mathbf{D}_μ stabilizations.

6. Numerical experiments

In this section, numerical experiments are conducted to demonstrate the accuracy, convergence and stability of the NVEM for compressible and nearly incompressible plane elasticity. The numerical results are compared with the B-bar virtual element (B-bar VEM) approach [2] and the standard linear VEM.

6.1. Colliding flow

We consider a simple model of colliding flow, which is a well-known and standard benchmark test problem (for example, see Refs. [60]) that can be solved using the linear elastostatic model

with the following constitutive matrix:

$$\mathbf{D} = \begin{bmatrix} \lambda + 2\mu & \lambda & 0 \\ \lambda & \lambda + 2\mu & 0 \\ 0 & 0 & \mu \end{bmatrix},$$

where the Lamé parameters are set to $\lambda = 5 \times 10^7$ and $\mu = 1$, thus resulting in a Poisson's ratio $\nu = 0.49999999$. The problem is defined on the square domain $\Omega = (0, 2)^2$ and possesses the following analytical solution [60]:

$$u_1 = 20(x_1 - 1)(x_2 - 1)^3 \quad (64a)$$

$$u_2 = 5(x_1 - 1)^4 - 5(x_2 - 1)^4 \quad (64b)$$

$$p = 60(x_1 - 1)^2(x_2 - 1) - 20(x_2 - 1)^3 \quad (64c)$$

Eqs. (64a) and (64b) are used as the Dirichlet boundary conditions along the boundary of the domain. The stabilizations presented in Section 5 are considered to assess the convergence of the method with mesh refinement. A sample polygonal mesh used in the convergence study is shown in Fig. 3.

We start by showing the need for stability in the NVEM approach. Fig. 4 presents a comparison between unstabilized and stabilized solutions for the nodal fields $\|\mathbf{u}_h\|$ and p_h — scatter plots are used for the NVEM as in this approach the field variables are known at the nodes. The unstabilized solutions exhibit marked spurious oscillations at the corners $(0, 0)$ and $(2, 0)$ (Figs. 4(a) and 4(c)), whereas the stabilized solutions become smooth on the whole domain (Figs. 4(b) and 4(d)).

The convergence and accuracy of the NVEM with $\tilde{\mathbf{D}}$ and \mathbf{D}_μ stabilizations is demonstrated in Fig. 5, where the L^2 norm and the H^1 seminorm of the displacement error, and the L^2 norm of the pressure error indicate accurate solutions with optimal convergence rates of 2, 1 and 1, respectively. In comparison with the B-bar VEM approach, which is also accurate and optimally convergent, the NVEM approach is slightly more accurate in the H^1 seminorm of the displacement error and the L^2 norm of the pressure error. Finally, as expected, in these convergence plots the

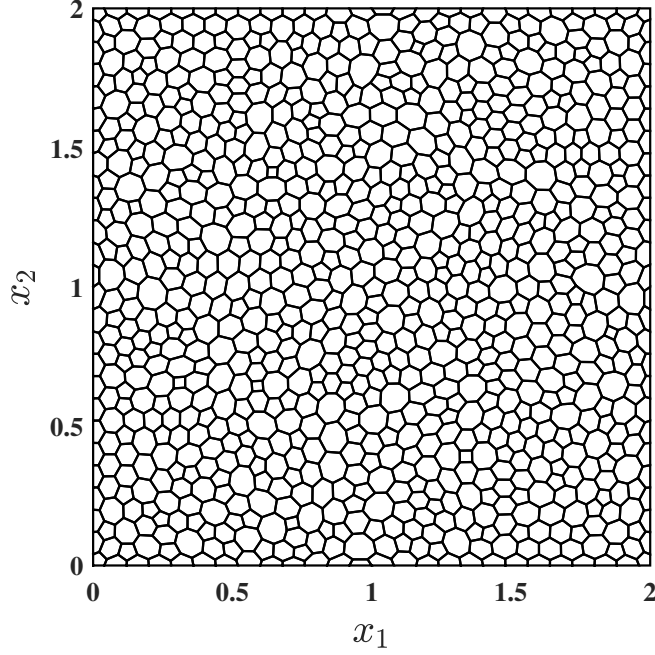


Fig. 3: Sample mesh for the colliding flow problem.

standard VEM solution behaves very inaccurate due to volumetric locking.

6.2. Cantilever beam subjected to a parabolic end load

A cantilever beam of unit thickness whose domain of analysis is $\Omega = (0, 8) \times (-2, 2)$ is subjected to a parabolic end load P that is applied on the edge $x = 8$. The essential boundary conditions are applied on the edge $x = 0$ according to the following exact solution given by Timoshenko and Goodier [61] for plane strain state:

$$u_1 = -\frac{Px_2}{6\bar{E}_Y I} \left((6L - 3x_1)x_1 + (2 + \bar{\nu})x_2^2 - \frac{3D^2}{2}(1 + \bar{\nu}) \right),$$

$$u_2 = \frac{P}{6\bar{E}_Y I} (3\bar{\nu}x_2^2(L - x_1) + (3L - x_1)x_1^2)$$

with $\bar{E}_Y = E_Y / (1 - \nu^2)$ and $\bar{\nu} = \nu / (1 - \nu)$, where E_Y and ν are the Young's modulus and Poisson's ratio of the linear elastic material; L is the length of the beam, D is the height of the beam, and I is the second-area moment of the beam section. The total load on the traction boundary is $P = -1000$. The geometry and boundary conditions, and a sample polygonal mesh

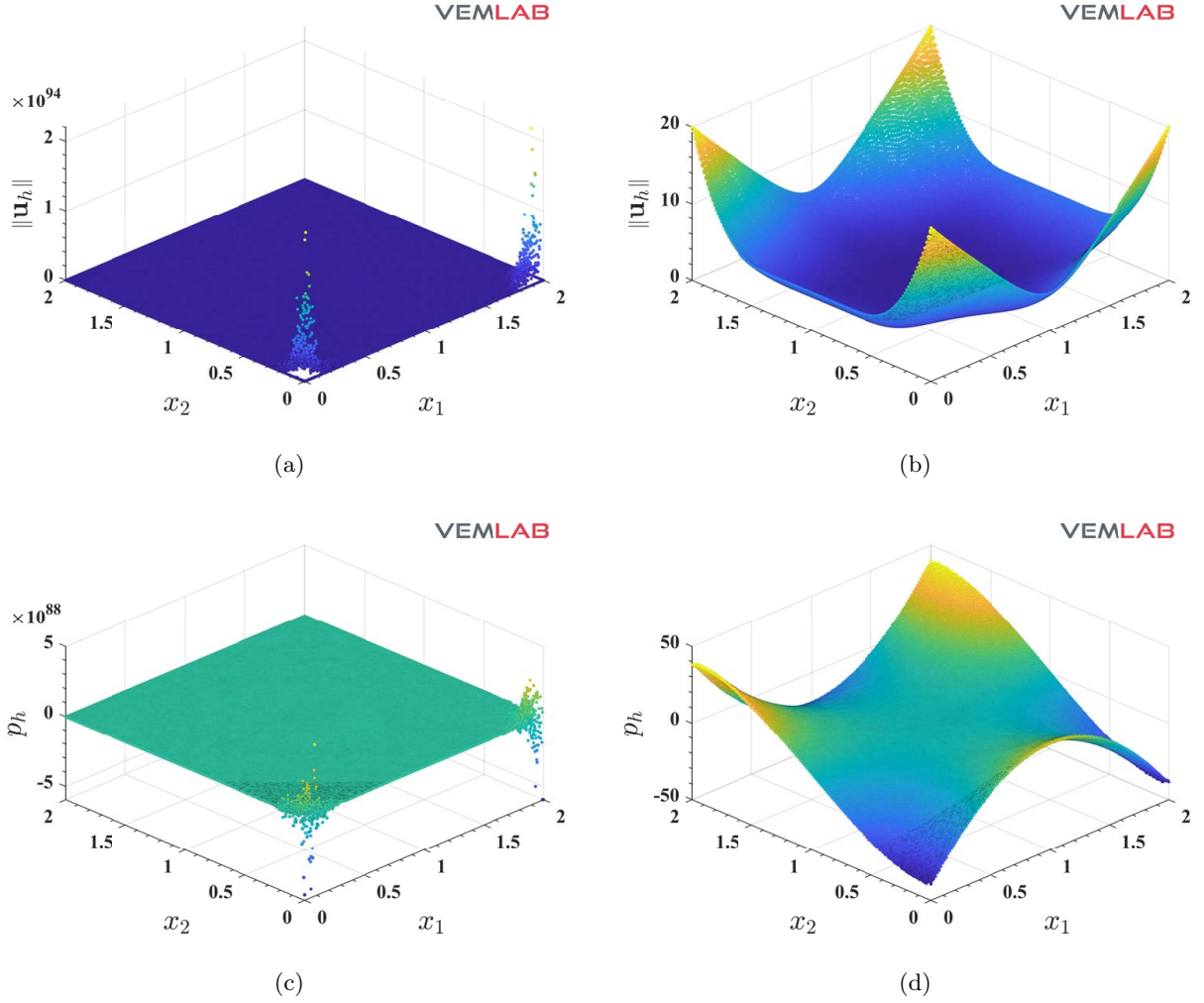


Fig. 4: Comparison between unstabilized and stabilized solutions in the NVEM for the colliding flow problem. (a) Unstabilized $\|\mathbf{u}_h\|$, (b) stabilized $\|\mathbf{u}_h\|$, (c) unstabilized $\|p_h\|$ and (d) stabilized $\|p_h\|$.

used in this study are shown in Fig. 6.

The convergence and accuracy of the NVEM is studied for two sets of material parameters. The first set is $E = 10^7$ and $\nu = 0.3$ (compressible elasticity), and the second set is $E = 10^7$ and $\nu = 0.499999$ (nearly incompressible elasticity).

6.2.1. Compressible elasticity

For compressible elasticity, Fig. 7 presents the L^2 norm and the H^1 seminorm of the displacement error, and the L^2 norm of the pressure error, where it is observed that accurate solutions with optimal convergence rates of 2, 1 and 1, respectively, are delivered by the NVEM with $\tilde{\mathbf{D}}$

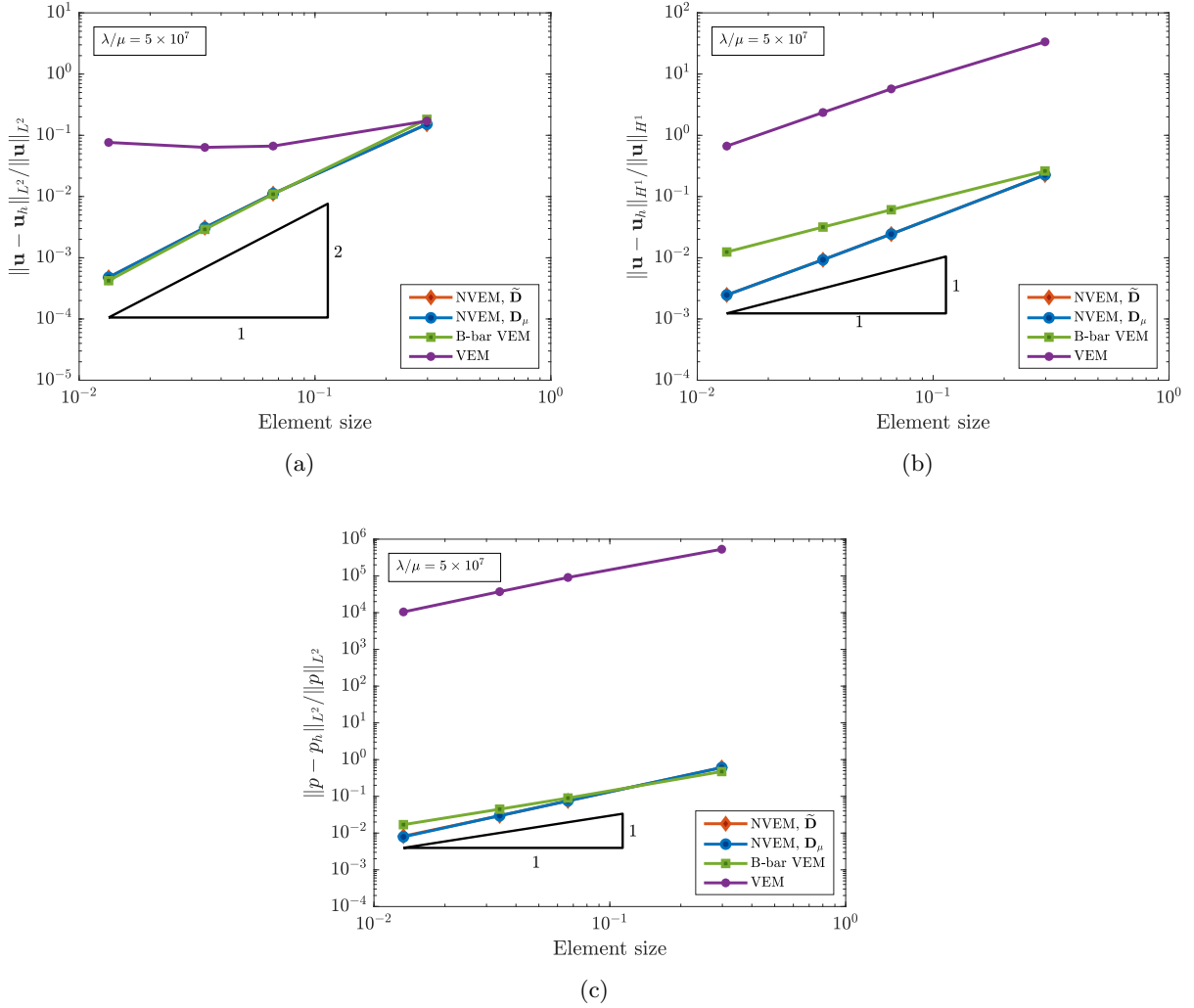


Fig. 5: Colliding flow problem. Convergence rates in the (a) L^2 norm of the displacement error, (b) H^1 seminorm of the displacement error and (c) L^2 norm of the pressure error for the VEM, B-bar VEM and NVEM.

and \mathbf{D}_μ stabilizations. The VEM and the B-bar VEM also exhibit accurate solutions with optimal rates of convergence. In comparison with the VEM and B-bar VEM, the NVEM is more accurate in the H^1 seminorm of the displacement error and the L^2 norm of the pressure error, whereas less accurate in the L^2 norm of the displacement error.

6.2.2. Nearly incompressible elasticity

For nearly incompressible elasticity, the NVEM and B-bar VEM are accurate and optimally convergent, as shown in Fig. 8. Like in the compressible case, the NVEM is more accurate than

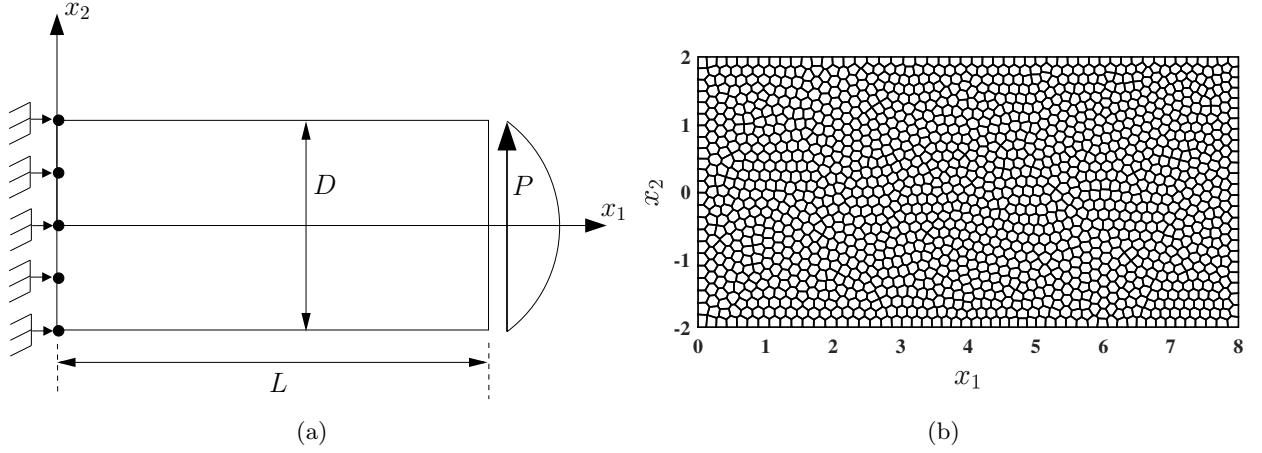


Fig. 6: Cantilever beam (a) geometry and boundary conditions, and (b) a sample mesh.

the B-bar VEM in the H^1 seminorm of the displacement error and the L^2 norm of the pressure error, whereas less accurate in the L^2 norm of the displacement error. Fig. 8 also shows that, as expected, the volumetric locking leads to inaccurate solutions and poor convergence in the VEM.

6.3. Cook's membrane

This standard benchmark problem is suitable to test the performance of numerical formulations for nearly incompressible solid materials under combined bending and shear. The left edge is clamped and the right end is subjected to a shear load $F = 6.25$ per unit length (total shear load of 100). The following material parameters are used: $E = 250$ and $\nu = 0.4999$. In this example, a non standard mesh is tested. To this end, we define a master multielement region formed by five polygons, as shown in Fig. 9, where the center polygon is an eight-point star known as ‘Guñelve’. This master multielement is mapped into the membrane geometry several times to form the mesh. The geometry and boundary conditions for the Cook's membrane problem and a sample ‘Guñelve’ mesh is shown in Fig. 10.

The convergence of the vertical tip displacement at point A upon mesh refinement is studied. For comparison purposes, a reference solution for the vertical tip displacement is found using a highly refined mesh of eight-node quadrilateral finite elements. The result of this study is summarized in Fig. 11, where it is shown that the B-bar VEM and NVEM solutions approach the reference value as the mesh is refined, and, as expected, the standard VEM exhibits very poor

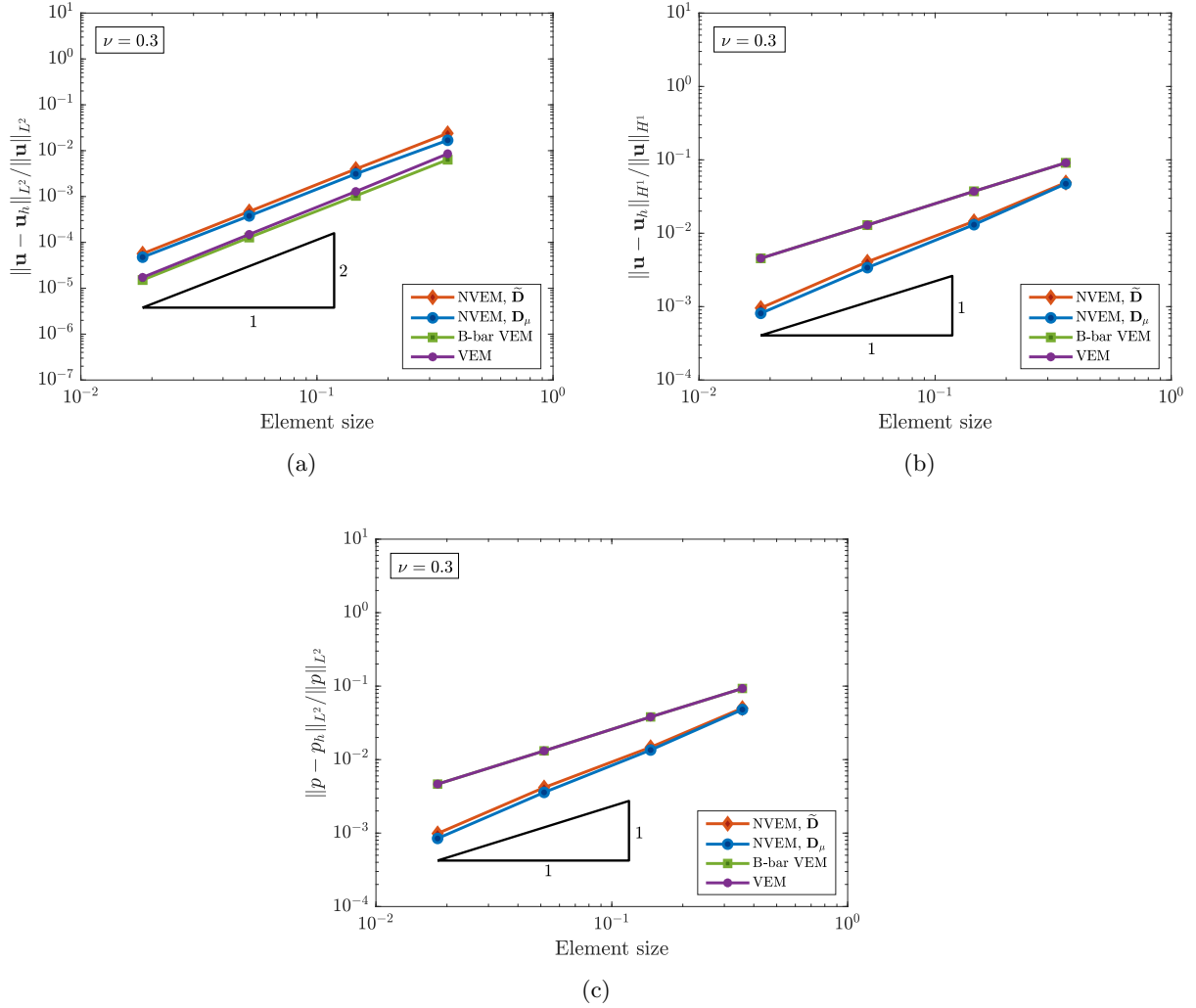


Fig. 7: Cantilever beam problem with material parameters $E_Y = 10^7$ and $\nu = 0.3$. Convergence rates in the (a) L^2 norm of the displacement error, (b) H^1 seminorm of the displacement error and (c) L^2 norm of the pressure error for the VEM, B-bar VEM and NVEM.

convergence due to volumetric locking.

Plots of the vertical displacement, pressure and von Mises stress fields are presented in Figs. 12, 13 and 14, respectively. Scatter plots are used for the NVEM as in this approach the field variables are known at the nodes. As expected, a very good agreement between the NVEM and B-bar VEM is observed in these plots.

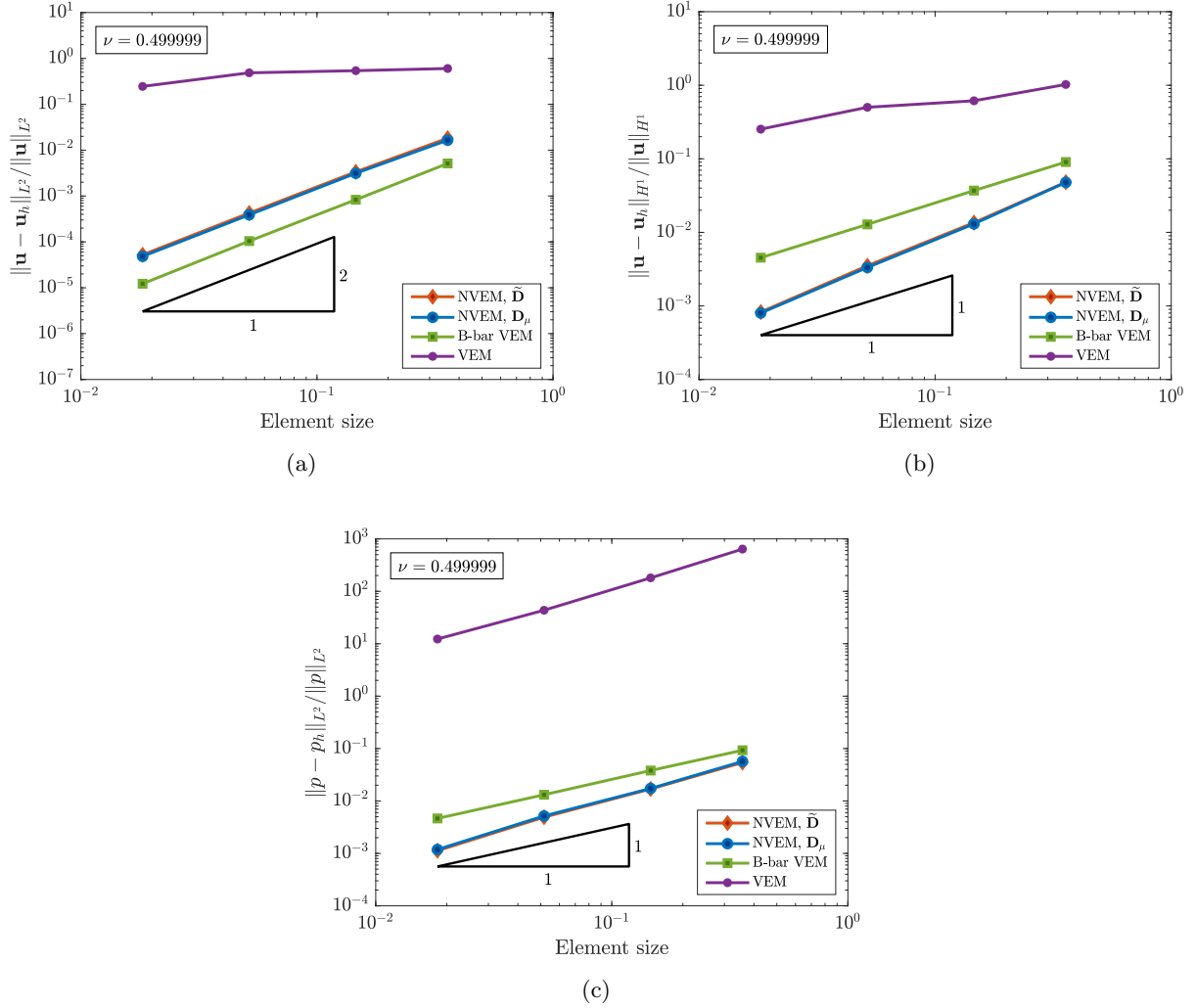


Fig. 8: Cantilever beam problem with material parameters $E_Y = 10^7$ and $\nu = 0.499999$. Convergence rates in the (a) L^2 norm of the displacement error, (b) H^1 seminorm of the displacement error and (c) L^2 norm of the pressure error for the VEM, B-bar VEM and NVEM.

6.4. Infinite plate with a circular hole

This example is devoted to study an infinite plate with a circular hole that is loaded at infinity with the following tractions: $\sigma_{11} = T$ and $\sigma_{22} = \sigma_{12} = 0$ (see Fig. 15(a)). Due to the symmetry of the geometry and boundary conditions, a quarter of the domain is used as the domain of analysis (see Fig. 15(b)). Plane stress and plane strain conditions are considered. For plane stress condition, the material parameters are set to $E_Y = 10^3$ and $\nu = 0.3$ (compressible elasticity), and for plane strain condition, they are set to $E_Y = 10^3$ and $\nu = 0.499999$ (nearly incompressible elasticity).

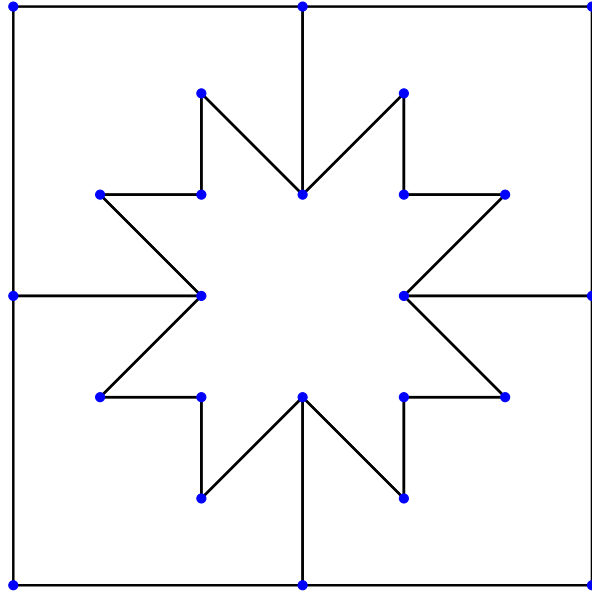


Fig. 9: Master multielement for the Cook's membrane problem. The center polygon defines an eight-point star known as 'Guñelve'.

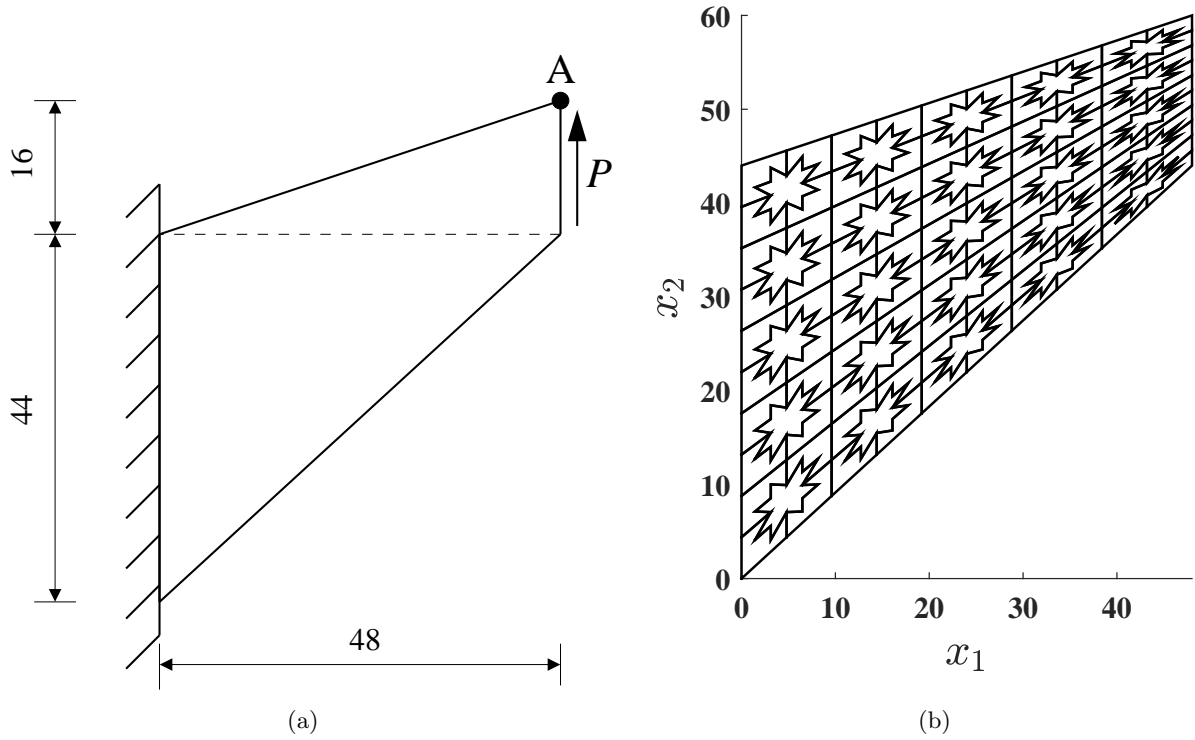


Fig. 10: Cook's membrane (a) geometry and boundary conditions, and (b) a sample 'Guñelve' mesh.

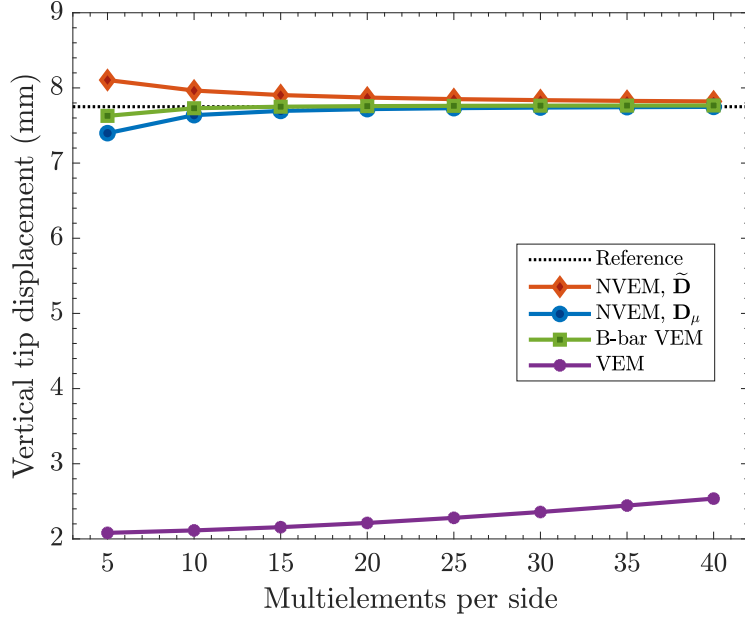


Fig. 11: Convergence of the vertical displacement at the tip of the Cook's membrane (point A) upon mesh refinement for the VEM, B-bar VEM and NVEM.

The exact solution is given by [61]

$$\mathbf{u} = \begin{bmatrix} \frac{T}{4G} \left(\frac{\kappa+1}{2} r \cos \theta + \frac{r_0^2}{r} \left((\kappa+1) \cos \theta + \cos 3\theta \right) - \frac{r_0^4}{r^3} \cos 3\theta \right) \\ \frac{T}{4G} \left(\frac{\kappa-3}{2} r \sin \theta + \frac{r_0^2}{r} \left((\kappa-1) \sin \theta + \sin 3\theta \right) - \frac{r_0^4}{r^3} \sin 3\theta \right) \end{bmatrix},$$

where $G = E_Y/(2(1+\nu))$ and $\kappa = (3-\nu)/(1+\nu)$. The exact stress field is

$$\begin{bmatrix} \sigma_{11} \\ \sigma_{22} \\ \sigma_{12} \end{bmatrix} = \begin{bmatrix} T \left(1 - \frac{r_0^2}{r^2} \left(\frac{3}{2} \cos 2\theta + \cos 4\theta \right) + \frac{3r_0^4}{2r^4} \cos 4\theta \right) \\ -T \left(\frac{r_0^2}{r^2} \left(\frac{1}{2} \cos 2\theta - \cos 4\theta \right) + \frac{3r_0^4}{2r^4} \cos 4\theta \right) \\ -T \left(\frac{r_0^2}{r^2} \left(\frac{1}{2} \sin 2\theta + \sin 4\theta \right) - \frac{3r_0^4}{2r^4} \sin 4\theta \right) \end{bmatrix},$$

where r is the radial distance from the center ($x_1 = 0, x_2 = 0$) to a point (x_1, x_2) in the domain of analysis. In the computations, the following data are used: $T = 100$, $r_0 = 1$ and $a = 5$. The Dirichlet boundary conditions on the domain of analysis (Fig. 15(b)) are imposed as follows: $u_{1D} = 0$ on the left side and $u_{2D} = 0$ on the bottom side. The Neumann boundary conditions are

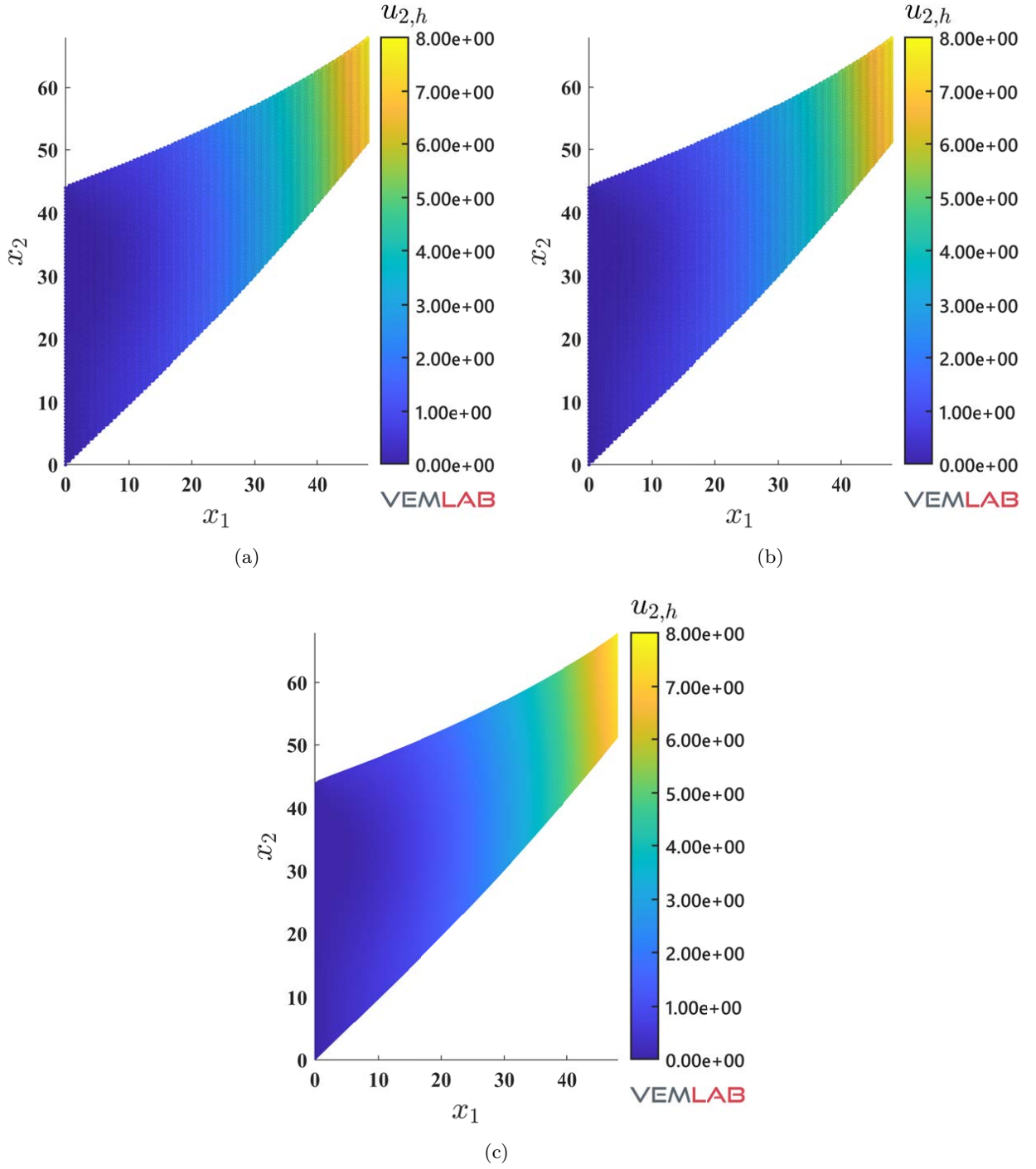


Fig. 12: Cook's membrane problem. Plots of the vertical displacement field solution ($u_{2,h}$) for the (a) NVEM ($\tilde{\mathbf{D}}$ stabilization), (b) NVEM (\mathbf{D}_μ stabilization) and (c) B-bar VEM approaches. Plots are deformed according to $u_{2,h}$.

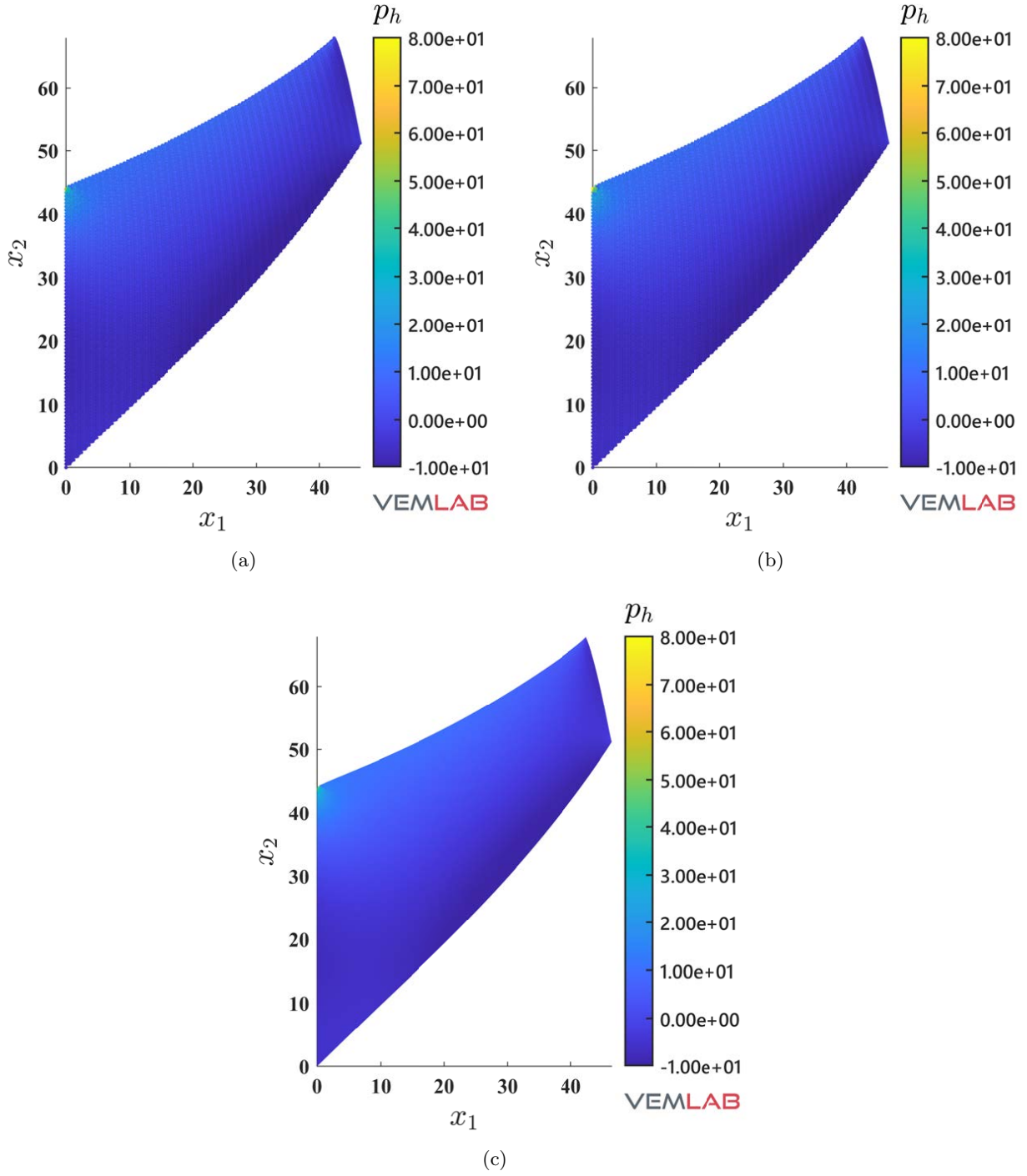


Fig. 13: Cook's membrane problem. Plots of the pressure field solution (p_h) for the (a) NVEM ($\tilde{\mathbf{D}}$ stabilization), (b) NVEM (\mathbf{D}_μ stabilization) and (c) B-bar VEM approaches. Plots are deformed according to $\|\mathbf{u}_h\|$.

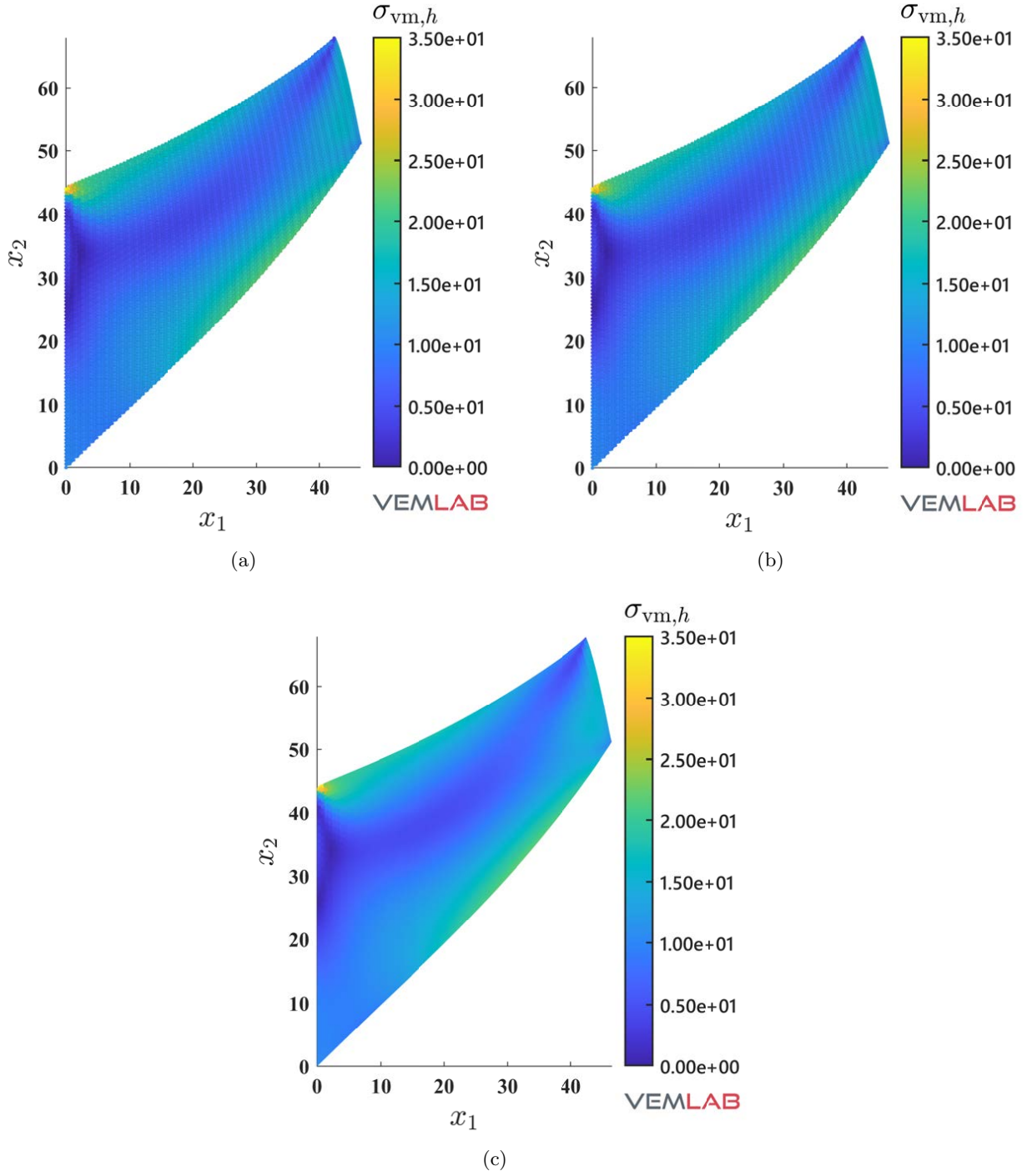


Fig. 14: Cook's membrane problem. Plots of the von Mises stress field solution ($\sigma_{vm,h}$) for the (a) NVEM ($\tilde{\mathbf{D}}$ stabilization), (b) NVEM (\mathbf{D}_μ stabilization) and (c) B-bar VEM approaches. Plots are deformed according to $\|\mathbf{u}_h\|$.

prescribed using the exact stresses, as follows: $\mathbf{t}_N = [t_{1N} \ t_{2N}]^T = [\sigma_{12} \ \sigma_{22}]^T$ on the top side and $\mathbf{t}_N = [t_{1N} \ t_{2N}]^T = [\sigma_{11} \ \sigma_{12}]^T$ on the right side.

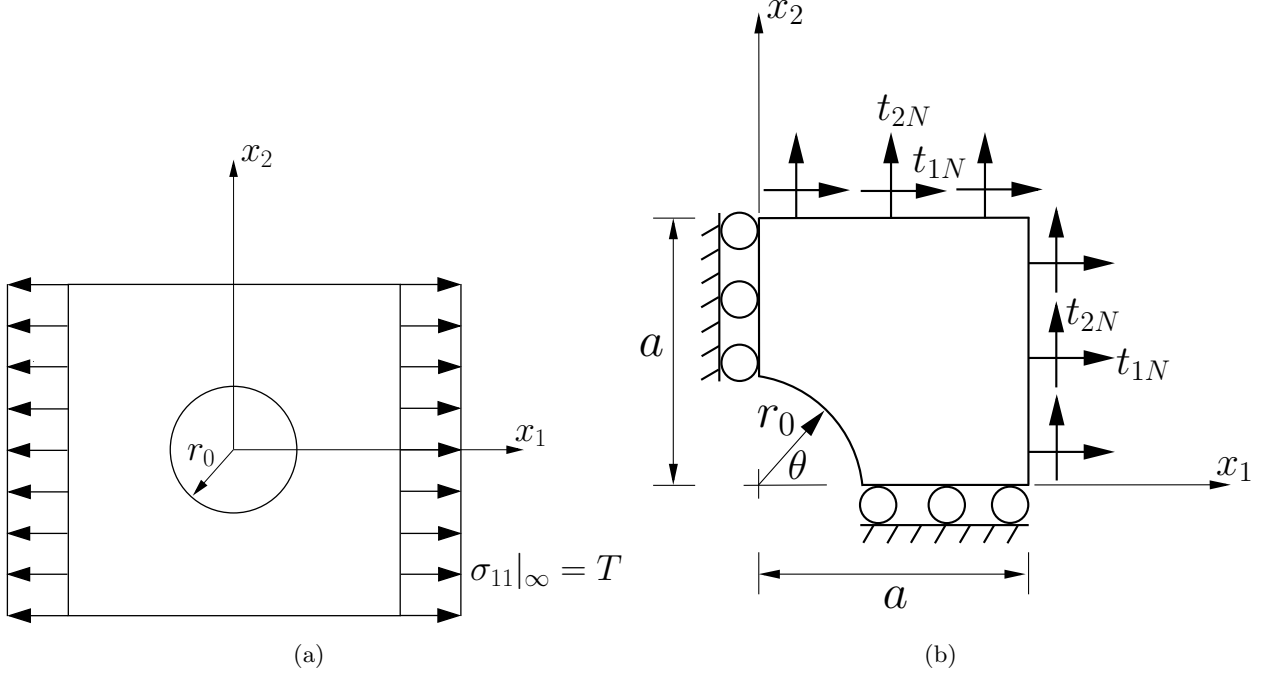


Fig. 15: Geometry and boundary conditions for the infinite plate with a circular hole. (a) Infinite domain and (b) a quarter of the domain.

In this example, regular, distorted and random meshes are used. For each of them, Fig. 16 shows a sample mesh. The random meshes are constructed from Delaunay tessellations using the longest edge propagation path and terminal-edge region concepts [62].

6.4.1. Compressible elasticity

In terms of accuracy and convergence upon mesh refinement, Fig. 17 reveals that for the compressible case on regular meshes all the methods are accurate and converge optimally in the L^2 norm and H^1 seminorm of the displacement error, and the L^2 norm of the pressure error (rates of 2, 1 and 1, respectively). In the L^2 norm of the displacement error, the VEM and B-bar VEM are more accurate than the NVEM. In the H^1 seminorm of the displacement error and the L^2 norm of the pressure error, the VEM, B-bar VEM and NVEM with $\tilde{\mathbf{D}}$ stabilization behave similar while the NVEM with \mathbf{D}_μ stabilization delivers the most accurate solution.

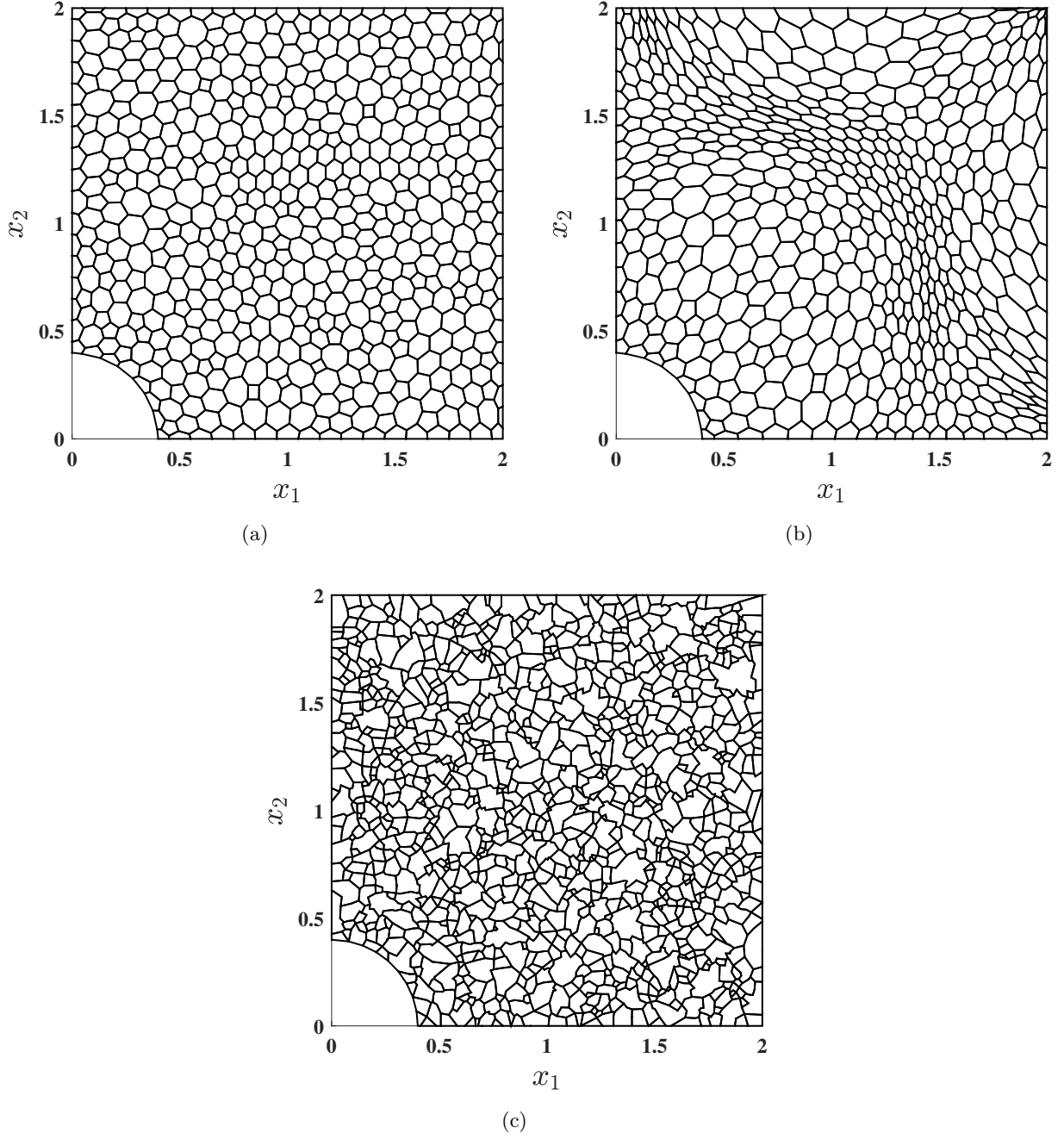


Fig. 16: Sample meshes for a quarter of the infinite plate with a circular hole. (a) Regular, (b) distorted, and (c) random meshes.

6.4.2. Nearly incompressible elasticity

For the nearly incompressible case, regular, distorted and random meshes are considered. On regular and distorted meshes, the B-bar VEM and NVEM are accurate and optimally convergent

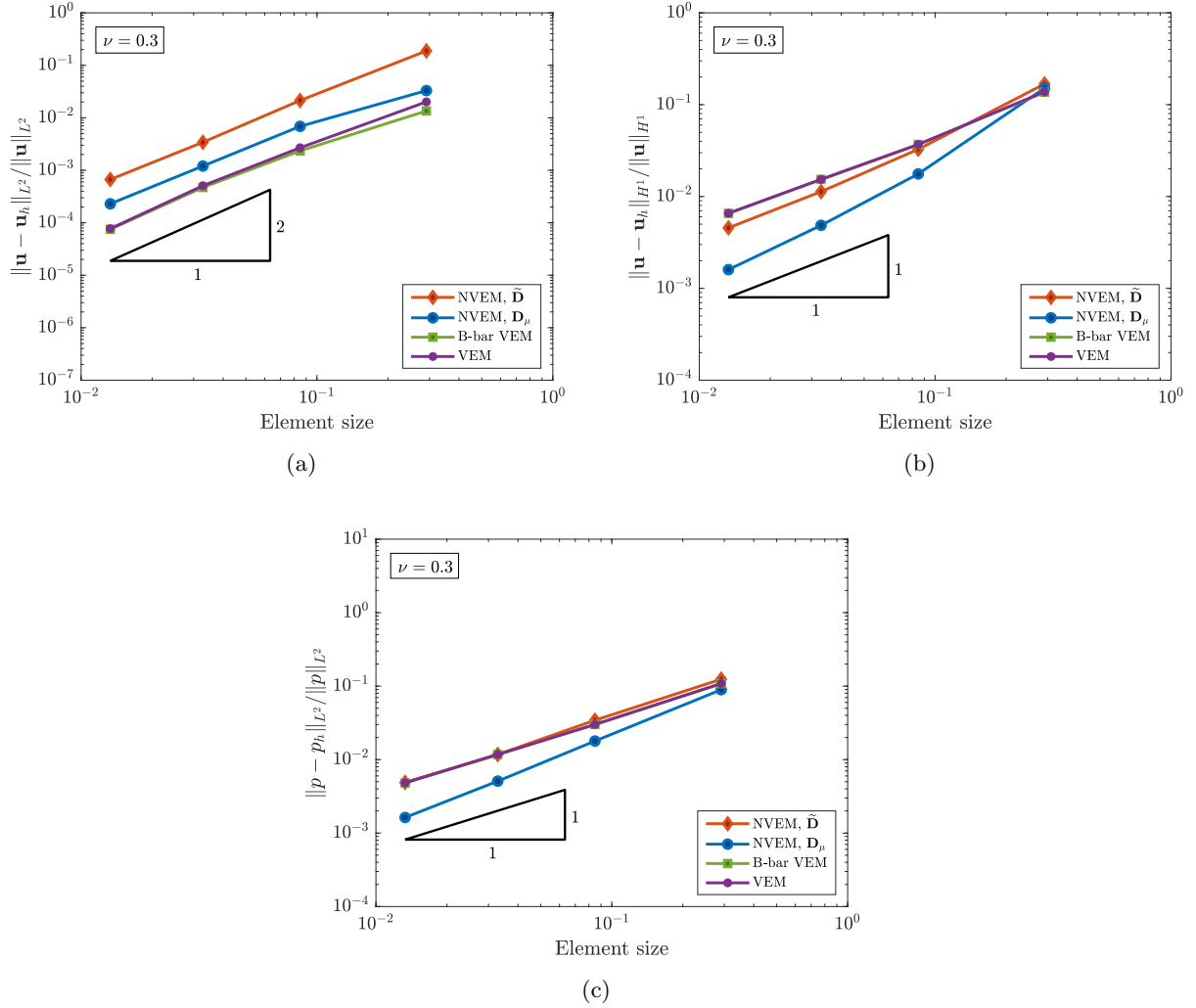


Fig. 17: Infinite plate with a circular hole problem on regular meshes. Material parameters $E_Y = 10^3$ and $\nu = 0.3$ for plane stress condition. Convergence rates in the (a) L^2 norm of the displacement error, (b) H^1 seminorm of the displacement error and (c) L^2 norm of the pressure error for the VEM, B-bar VEM and NVEM.

in the three norms (see Figs. 18 and 19), whereas, as expected, the VEM is severely inaccurate due to volumetric locking. In comparison with the B-bar VEM, Figs. 18 and 19 show that the NVEM is slightly more accurate in the H^1 seminorm of the displacement error and the L^2 norm of the pressure error, whereas less accurate in the L^2 norm of the displacement error. We also observe that between the two stabilized NVEM, the NVEM with \mathbf{D}_μ stabilization is slightly more accurate.

On random meshes, the B-bar VEM and NVEM are accurate and optimally convergent in

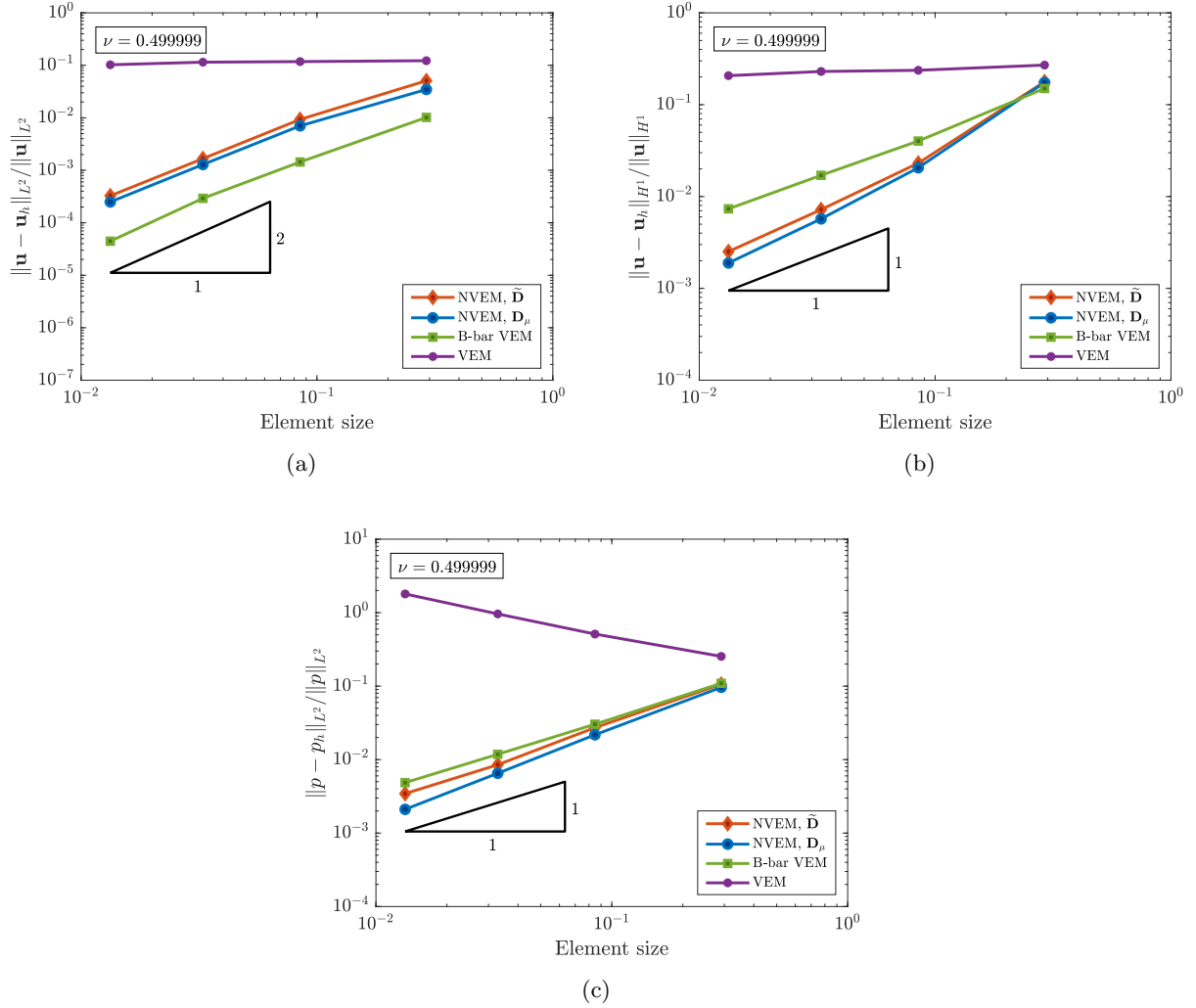


Fig. 18: Infinite plate with a circular hole problem on regular meshes. Material parameters $E_Y = 10^3$ and $\nu = 0.499999$ for plane strain condition. Convergence rates in the (a) L^2 norm of the displacement error, (b) H^1 seminorm of the displacement error and (c) L^2 norm of the pressure error for the VEM, B-bar VEM and NVEM.

the three norms (Fig. 20), whereas the VEM is severely inaccurate due to volumetric locking. Fig. 20(a) reveals that in the L^2 norm of the displacement error the NVEM with $\tilde{\mathbf{D}}$ stabilization is less accurate than the B-bar VEM, whereas slightly more accurate when \mathbf{D}_μ stabilization is used. Regarding the H^1 seminorm of the displacement error, Fig. 20(b) shows that the B-bar VEM and NVEM with $\tilde{\mathbf{D}}$ stabilization behave similar while the NVEM with \mathbf{D}_μ stabilization is the most accurate. With respect to the L^2 norm of the pressure error, the B-bar VEM is slightly more accurate than the NVEM approach (Fig. 20(c)).

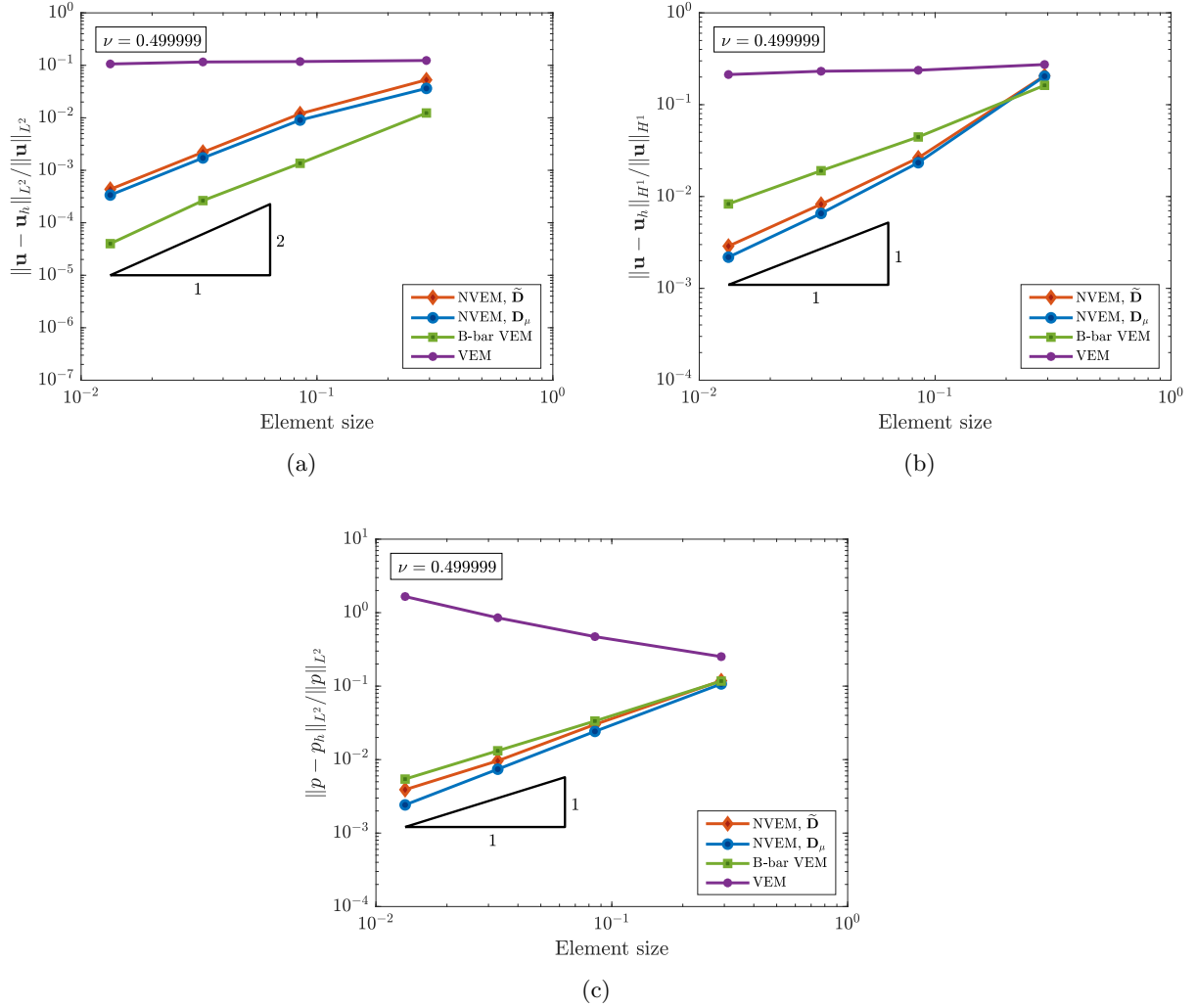


Fig. 19: Infinite plate with a circular hole problem on distorted meshes. Material parameters $E_Y = 10^3$ and $\nu = 0.499999$ for plane strain condition. Convergence rates in the (a) L^2 norm of the displacement error, (b) H^1 seminorm of the displacement error and (c) L^2 norm of the pressure error for the VEM, B-bar VEM and NVEM.

Finally, plots of the displacement, pressure and von Mises stress fields are presented in Figs. 21, 22 and 23, respectively. Scatter plots are used for the NVEM as in this approach the field variables are known at the nodes. A very good agreement between the NVEM and B-bar VEM solutions is found in these plots.

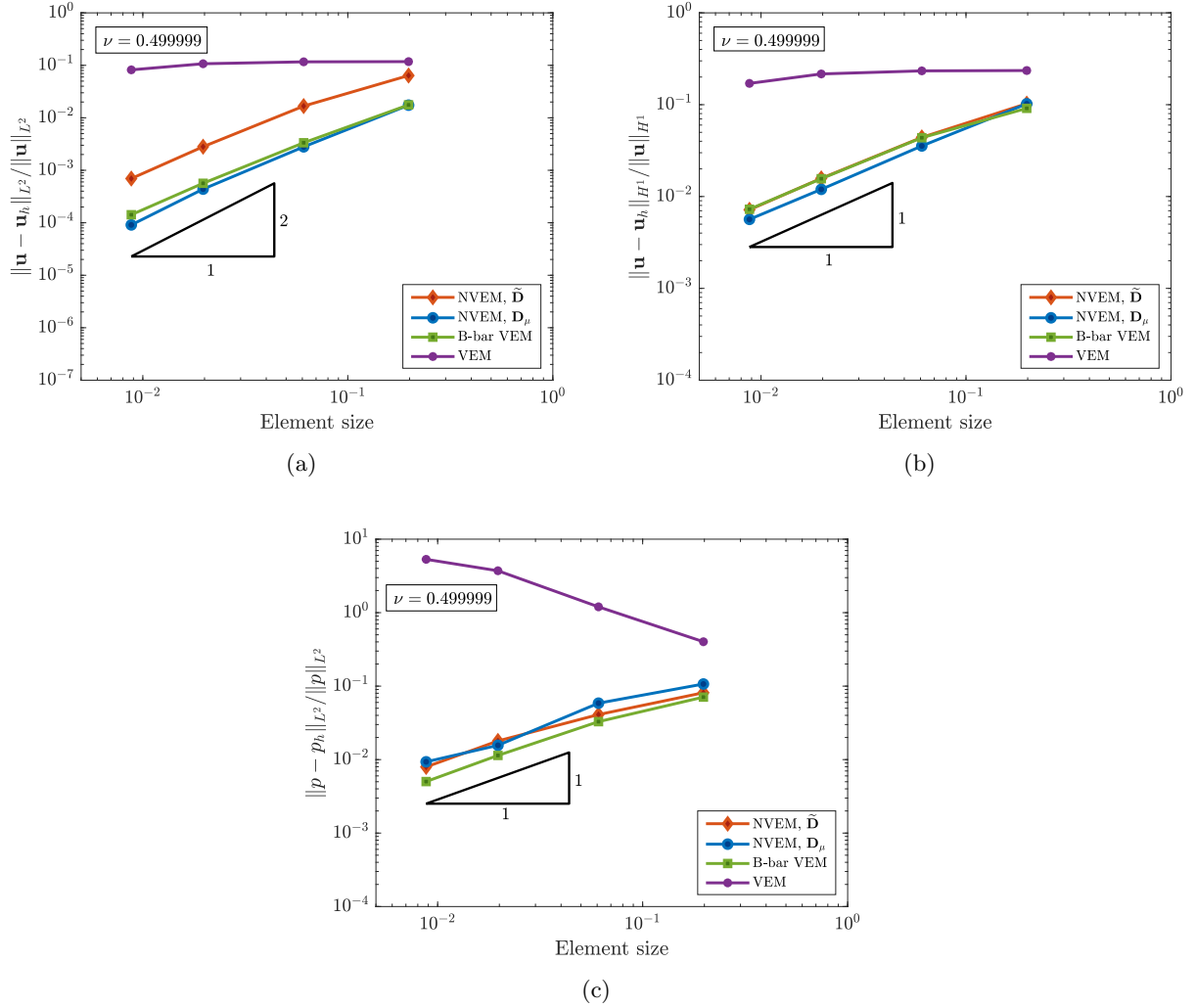


Fig. 20: Infinite plate with a circular hole problem on random meshes. Material parameters $E_Y = 10^3$ and $\nu = 0.499999$ for plane strain condition. Convergence rates in the (a) L^2 norm of the displacement error, (b) H^1 seminorm of the displacement error and (c) L^2 norm of the pressure error for the VEM, B-bar VEM and NVEM.

7. Concluding remarks

In this paper, we proposed a combined nodal integration and virtual element method, wherein the strain is averaged around nodes from the strain of surrounding virtual elements. For the strain averaging procedure, a nodal averaging operator was constructed using a generalization to virtual elements of the node-based uniform strain approach for finite elements [34]. This gave rise to new virtual elements, which are termed node-based uniform strain virtual elements (NVEM). Two stabilizations were proposed for the NVEM in line with nodal integration techniques, where the

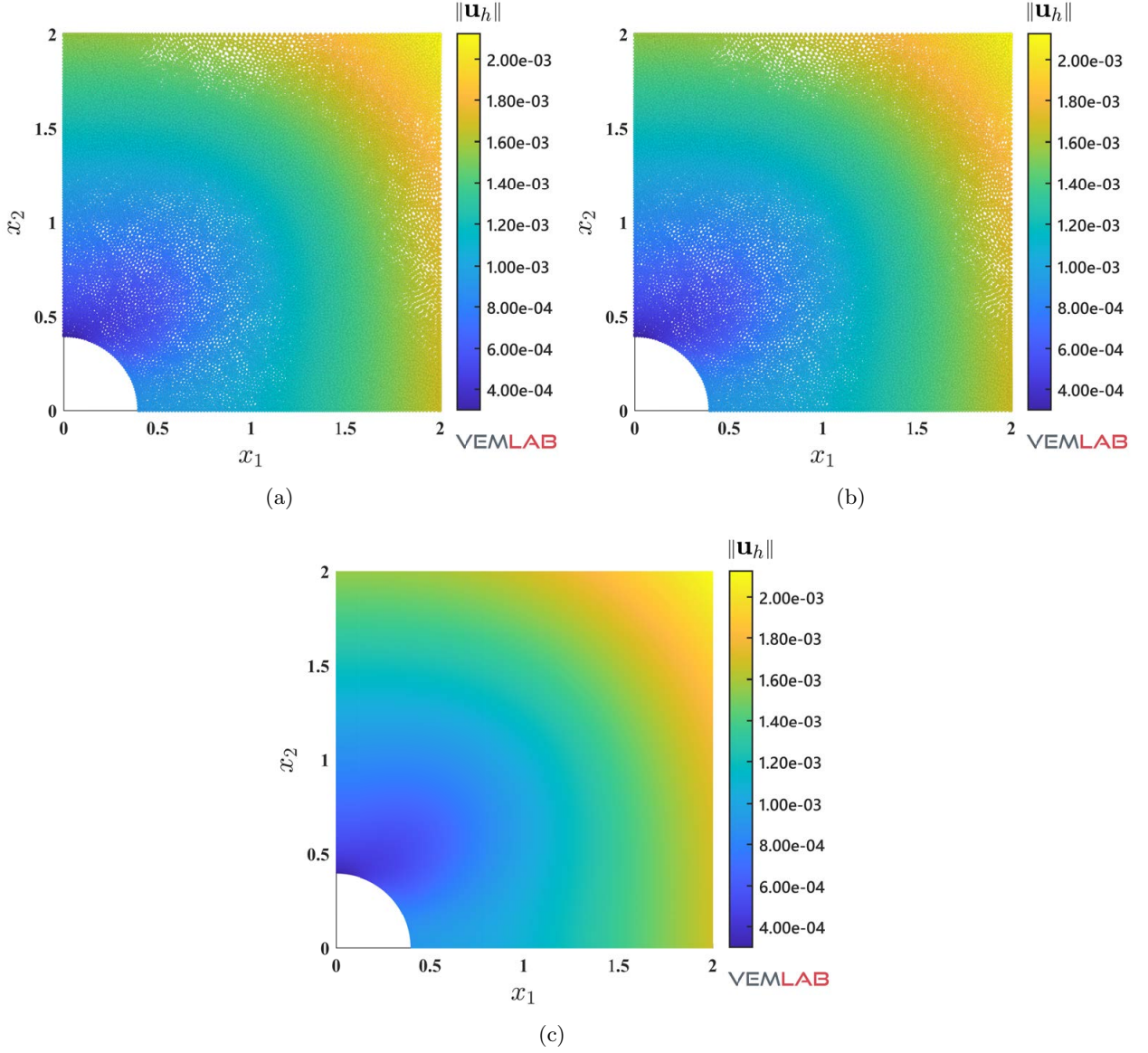


Fig. 21: Infinite plate with a circular hole problem on distorted meshes. Material parameters $E_Y = 10^3$ and $\nu = 0.499999$ for plane strain condition. Plots of the resultant displacement field solution ($\|\mathbf{u}_h\|$) for the (a) NVEM ($\tilde{\mathbf{D}}$ stabilization), (b) NVEM (\mathbf{D}_μ stabilization) and (c) B-bar VEM approaches.

stabilizations are constructed using a modified constitutive matrix. The main distinction of the NVEM from existing VEM approaches for compressible and nearly incompressible elasticity, such as the B-Bar VEM [2], is that the stresses and strains are nodal variables just like displacements, whereas in the existing methods the stresses and strains are element variables.

Several examples in compressible and nearly incompressible elasticity were conducted using

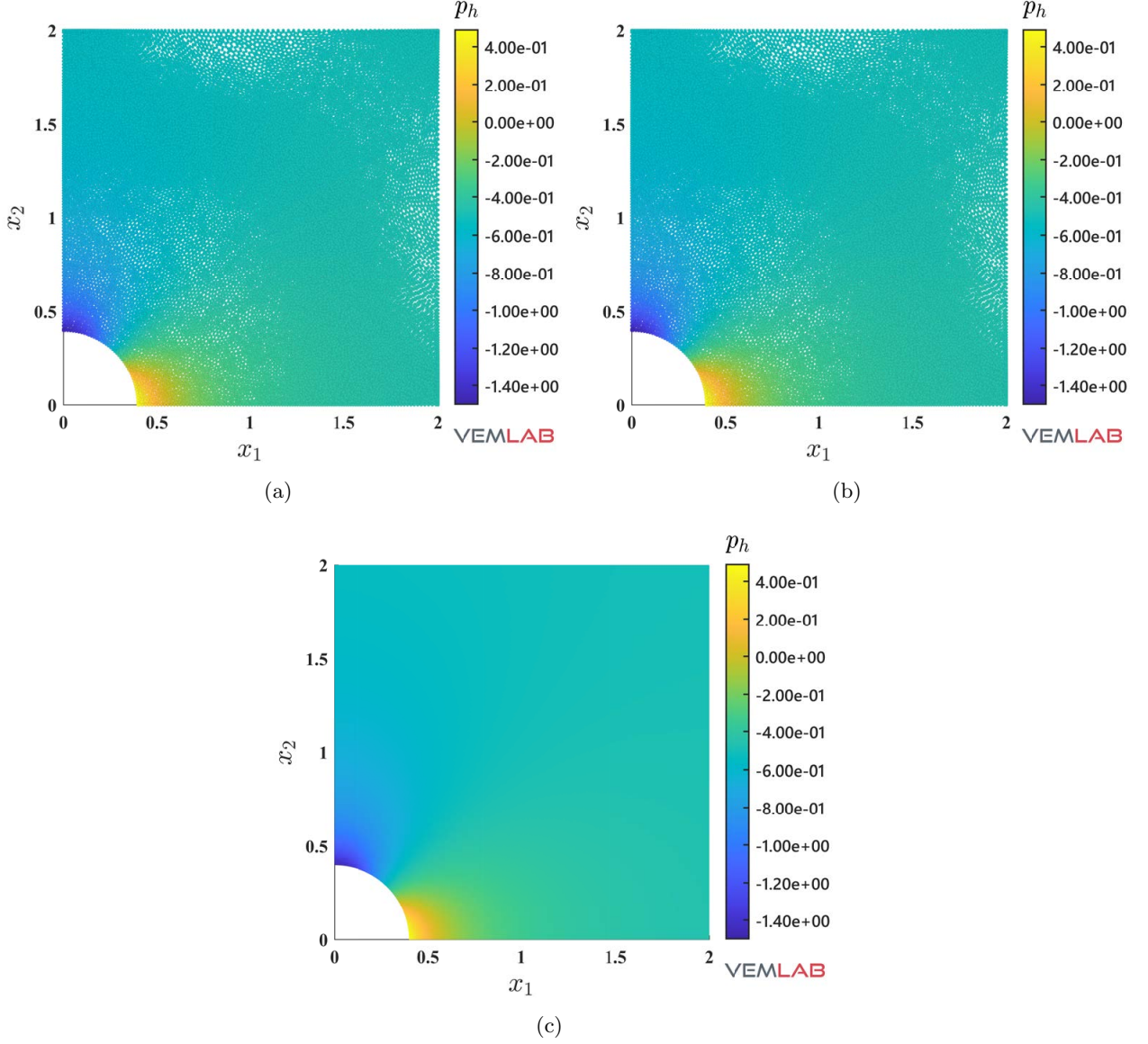


Fig. 22: Infinite plate with a circular hole problem on distorted meshes. Material parameters $E_Y = 10^3$ and $\nu = 0.499999$ for plane strain condition. Plots of the pressure field solution (p_h) for the (a) NVEM ($\tilde{\mathbf{D}}$ stabilization), (b) NVEM (\mathbf{D}_μ stabilization) and (c) B-bar VEM approaches.

regular, distorted and random discretizations in two dimensions. The NVEM showed accurate, convergent and stable solutions in the L^2 norm and H^1 seminorm of the displacement error in all the numerical tests. Even though the NVEM and the B-Bar VEM are in good agreement, we remark that all the field variables in the NVEM are related to the nodes, which obviously would ease the tracking of state and history-dependent variables in the nonlinear regime. Also,

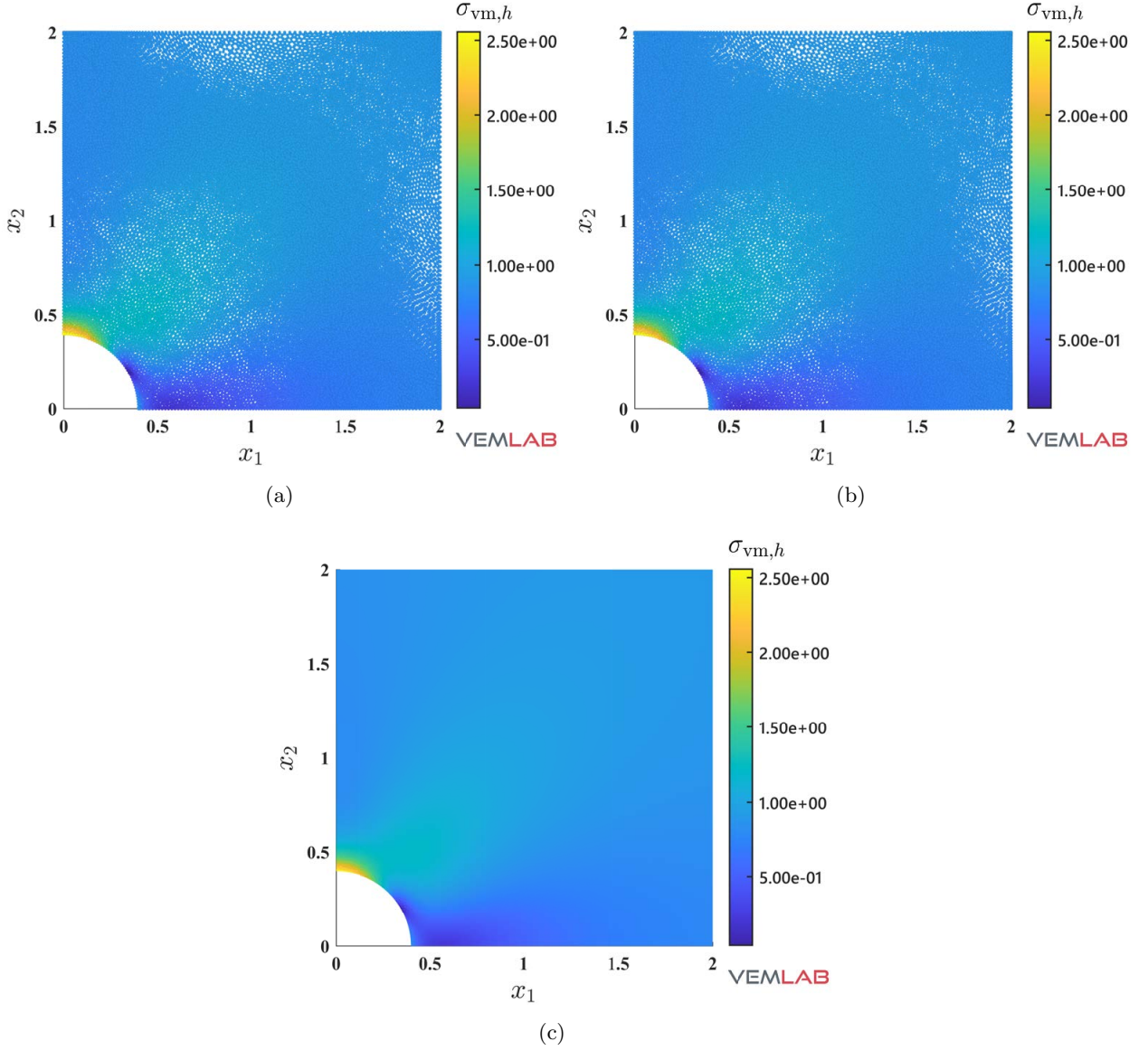


Fig. 23: Infinite plate with a circular hole problem on distorted meshes. Material parameters $E_Y = 10^3$ and $\nu = 0.499999$ for plane strain condition. Plots of the von Mises stress field solution ($\sigma_{vm,h}$) for the (a) NVEM ($\bar{\mathbf{D}}$ stabilization), (b) NVEM (\mathbf{D}_μ stabilization) and (c) B-bar VEM approaches.

the nodal character of these variables can be exploited in extreme deformations settings, where, if remeshing is needed, a remeshing strategy using the current set of nodes would eliminate the necessity of remapping of state and history-dependent variables between the old and new meshes. The aforementioned features provide room for further development of the NVEM. In a short term view, our current work on the NVEM is focused on its extension to materially-nonlinear-only

formulation. In the medium term, we plan to develop its extension to finite deformations.

Acknowledgements

The authors acknowledge the research support of the Chilean National Fund for Scientific and Technological Development (FONDECYT) through grant ANID FONDECYT No. 1221325.

References

- [1] K. Park, H. Chi, G. H. Paulino, Numerical recipes for elastodynamic virtual element methods with explicit time integration, *International Journal for Numerical Methods in Engineering* 121 (1) (2020) 1–31.
- [2] K. Park, H. Chi, G. H. Paulino, B-bar virtual element method for nearly incompressible and compressible materials, *Meccanica* 56 (6) (2021) 1423–1439.
- [3] E. Artioli, S. de Miranda, C. Lovadina, L. Patruno, A stress/displacement virtual element method for plane elasticity problems, *Computer Methods in Applied Mechanics and Engineering* 325 (2017) 155–174.
- [4] A. D’Altri, S. de Miranda, L. Patruno, E. Sacco, An enhanced vem formulation for plane elasticity, *Computer Methods in Applied Mechanics and Engineering* 376 (2021) 113663.
- [5] F. Dassi, C. Lovadina, M. Visinoni, Hybridization of the virtual element method for linear elasticity problems, *Mathematical Models and Methods in Applied Sciences* 31 (14) (2021) 2979–3008.
- [6] D. Y. Kwak, H. Park, Lowest-order virtual element methods for linear elasticity problems, *Computer Methods in Applied Mechanics and Engineering* 390 (2022) 114448.
- [7] B. Zhang, J. Zhao, Y. Yang, S. Chen, The nonconforming virtual element method for elasticity problems, *Journal of Computational Physics* 378 (2019) 394–410.
- [8] Y. Yu, A lowest-order locking-free nonconforming virtual element method based on the reduced integration technique for linear elasticity problems (2021). [doi:10.48550/ARXIV.2112.13378](https://doi.org/10.48550/ARXIV.2112.13378).
- [9] X. Tang, Z. Liu, B. Zhang, M. Feng, A low-order locking-free virtual element for linear elasticity problems, *Computers & Mathematics with Applications* 80 (5) (2020) 1260–1274.
- [10] S. Beissel, T. Belytschko, Nodal integration of the element-free Galerkin method, *Computer Methods in Applied Mechanics and Engineering* 139 (1) (1996) 49–74.
- [11] M. A. Puso, J.-S. Chen, E. Zywicz, W. Elmer, Meshfree and finite element nodal integration methods, *International Journal for Numerical Methods in Engineering* 74 (3) (2008) 416–446.
- [12] M. M. Rashid, Material state remapping in computational solid mechanics, *International Journal for Numerical Methods in Engineering* 55 (4) (2002) 431–450.
- [13] N.-S. Lee, K.-J. Bathe, Error indicators and adaptive remeshing in large deformation finite element analysis, *Finite Elements in Analysis and Design* 16 (2) (1994) 99–139.

- [14] G. Camacho, M. Ortiz, Adaptive lagrangian modelling of ballistic penetration of metallic targets, *Computer Methods in Applied Mechanics and Engineering* 142 (3) (1997) 269–301.
- [15] V. Vavourakis, D. Loukidis, D. C. Charmpis, P. Papanastasiou, Assessment of remeshing and remapping strategies for large deformation elastoplastic finite element analysis, *Computers & Structures* 114–115 (2013) 133–146.
- [16] T. Belytschko, S. Xiao, Stability analysis of particle methods with corrected derivatives, *Computers & Mathematics with Applications* 43 (3–5) (2002) 329–350.
- [17] T. P. Fries, T. Belytschko, Convergence and stabilization of stress-point integration in mesh-free and particle methods, *International Journal for Numerical Methods in Engineering* 74 (7) (2008) 1067–1087.
- [18] T. Belytschko, Y. Guo, W. K. Liu, S. P. Xiao, A unified stability analysis of meshless particle methods, *International Journal for Numerical Methods in Engineering* 48 (9) (2000) 1359–1400.
- [19] M. Hillman, J.-S. Chen, An accelerated, convergent, and stable nodal integration in Galerkin meshfree methods for linear and nonlinear mechanics, *International Journal for Numerical Methods in Engineering* 107 (7) (2016) 603–630.
- [20] J.-S. Chen, M. Hillman, M. Rüter, An arbitrary order variationally consistent integration for Galerkin meshfree methods, *International Journal for Numerical Methods in Engineering* 95 (5) (2013) 387–418.
- [21] M. A. Puso, J. Solberg, A stabilized nodally integrated tetrahedral, *International Journal for Numerical Methods in Engineering* 67 (6) (2006) 841–867.
- [22] J.-S. Chen, C. T. Wu, S. Yoon, Y. You, A stabilized conforming nodal integration for Galerkin mesh-free methods, *International Journal for Numerical Methods in Engineering* 50 (2) (2001) 435–466.
- [23] J.-S. Chen, S. Yoon, C. T. Wu, Non-linear version of stabilized conforming nodal integration for Galerkin mesh-free methods, *International Journal for Numerical Methods in Engineering* 53 (12) (2002) 2587–2615.
- [24] W. Elmer, J. S. Chen, M. Puso, E. Tacioglu, A stable, meshfree, nodal integration method for nearly incompressible solids, *Finite Elements in Analysis and Design* 51 (2012) 81–85.
- [25] R. Silva-Valenzuela, A. Ortiz-Bernardin, N. Sukumar, E. Artioli, N. Hitschfeld-Kahler, A nodal integration scheme for meshfree galerkin methods using the virtual element decomposition, *International Journal for Numerical Methods in Engineering* 121 (10) (2020) 2174–2205.
- [26] Q. Duan, B. Wang, X. Gao, X. Li, Quadratically consistent nodal integration for second order meshfree Galerkin methods, *Computational Mechanics* 54 (2) (2014) 353–368.
- [27] P. Lancaster, K. Salkauskas, Surfaces generated by moving least squares methods, *Mathematics of Computations* 37 (1981) 141–158.
- [28] T. Belytschko, Y. Y. Lu, L. Gu, Element-free Galerkin methods, *International Journal for Numerical Methods in Engineering* 37 (2) (1994) 229–256.
- [29] W. K. Liu, S. Jun, Y. F. Zhang, Reproducing kernel particle methods, *International Journal for Numerical Methods in Engineering* 20 (8–9) (1995) 1081–1106.
- [30] N. Sukumar, Construction of polygonal interpolants: a maximum entropy approach, *International Journal for*

Numerical Methods in Engineering 61 (12) (2004) 2159–2181.

- [31] N. Sukumar, R. W. Wright, Overview and construction of meshfree basis functions: from moving least squares to entropy approximants, *International Journal for Numerical Methods in Engineering* 70 (2) (2007) 181–205.
- [32] M. Arroyo, M. Ortiz, Local maximum-entropy approximation schemes: a seamless bridge between finite elements and meshfree methods, *International Journal for Numerical Methods in Engineering* 65 (13) (2006) 2167–2202.
- [33] J. Bonet, A. J. Burton, A simple average nodal pressure tetrahedral element for incompressible and nearly incompressible dynamic explicit applications, *Communications in Numerical Methods in Engineering* 14 (5) (1998) 437–449.
- [34] C. R. Dohrmann, M. W. Heinstein, J. Jung, S. W. Key, W. R. Witkowski, Node-based uniform strain elements for three-node triangular and four-node tetrahedral meshes, *International Journal for Numerical Methods in Engineering* 47 (9) (2000) 1549–1568.
- [35] J. Bonet, H. Marriott, O. Hassan, An averaged nodal deformation gradient linear tetrahedral element for large strain explicit dynamic applications, *Communications in Numerical Methods in Engineering* 17 (8) (2001) 551–561.
- [36] P. Krysl, B. Zhu, Locking-free continuum displacement finite elements with nodal integration, *International Journal for Numerical Methods in Engineering* 76 (7) (2008) 1020–1043.
- [37] G. Castellazzi, P. Krysl, Displacement-based finite elements with nodal integration for reissner–mindlin plates, *International Journal for Numerical Methods in Engineering* 80 (2) (2009) 135–162.
- [38] P. Krysl, H. Kagey, Reformulation of nodally integrated continuum elements to attain insensitivity to distortion, *International Journal for Numerical Methods in Engineering* 90 (7) (2012) 805–818.
- [39] G. Castellazzi, P. Krysl, Patch-averaged assumed strain finite elements for stress analysis, *International Journal for Numerical Methods in Engineering* 90 (13) (2012) 1618–1635.
- [40] M. Broccardo, M. Micheloni, P. Krysl, Assumed-deformation gradient finite elements with nodal integration for nearly incompressible large deformation analysis, *International Journal for Numerical Methods in Engineering* 78 (9) (2009) 1113–1134.
- [41] G. Castellazzi, P. Krysl, I. Bartoli, A displacement-based finite element formulation for the analysis of laminated composite plates, *Composite Structures* 95 (2013) 518–527.
- [42] E. Artioli, G. Castellazzi, P. Krysl, Assumed strain nodally integrated hexahedral finite element formulation for elastoplastic applications, *International Journal for Numerical Methods in Engineering* 99 (11) (2014) 844–866.
- [43] A. Franci, M. Cremonesi, U. Perego, E. O. nate, A lagrangian nodal integration method for free-surface fluid flows, *Computer Methods in Applied Mechanics and Engineering* 361 (2020) 112816.
- [44] J. Meng, X. Zhang, S. Utili, E. O. nate, A nodal-integration based particle finite element method (N-PFEM) to model cliff recession, *Geomorphology* 381 (2021) 107666.
- [45] A. Ortiz-Bernardin, C. Alvarez, N. Hitschfeld-Kahler, A. Russo, R. Silva-Valenzuela, E. Olate-Sanzana, Veamy: an extensible object-oriented C++ library for the virtual element method, *Numerical Algorithms* 82 (4) (2019)

1189–1220.

- [46] E. Artioli, L. Beirão da Veiga, C. Lovadina, E. Sacco, Arbitrary order 2D virtual elements for polygonal meshes: part I, elastic problem, *Computational Mechanics* 60 (3) (2017) 355–377.
- [47] E. Artioli, L. Beirão da Veiga, C. Lovadina, E. Sacco, Arbitrary order 2D virtual elements for polygonal meshes: part II, inelastic problem, *Computational Mechanics* 60 (4) (2017) 643–657.
- [48] P. Wriggers, B. D. Reddy, W. Rust, B. Hudobivnik, Efficient virtual element formulations for compressible and incompressible finite deformations, *Computational Mechanics* 60 (2) (2017) 253–268.
- [49] L. Beirão da Veiga, F. Dassi, A. Russo, High-order virtual element method on polyhedral meshes, *Computers & Mathematics with Applications* 74 (5) (2017) 1110–1122.
- [50] L. Beirão da Veiga, F. Brezzi, F. Dassi, L. D. Marini, A. Russo, Serendipity virtual elements for general elliptic equations in three dimensions, *Chinese Annals of Mathematics, Series B* 39 (2018) 315–334.
- [51] K. Park, H. Chi, G. H. Paulino, On nonconvex meshes for elastodynamics using virtual element methods with explicit time integration, *Computer Methods in Applied Mechanics and Engineering* 356 (2019) 669–684.
- [52] H. Chi, L. B. da Veiga, G. Paulino, Some basic formulations of the virtual element method (VEM) for finite deformations, *Computer Methods in Applied Mechanics and Engineering* 318 (2017) 148–192.
- [53] A. L. Gain, G. H. Paulino, Bridging art and engineering using escher-based virtual elements, *Structural and Multidisciplinary Optimization* 51 (2015) 867–883.
- [54] L. Beirão da Veiga, F. Brezzi, A. Cangiani, G. Manzini, L. D. Marini, A. Russo, Basic principles of virtual element methods, *Mathematical Models and Methods in Applied Sciences* 23 (1) (2013) 199–214.
- [55] A. L. Gain, C. Talischi, G. H. Paulino, On the virtual element method for three-dimensional linear elasticity problems on arbitrary polyhedral meshes, *Computer Methods in Applied Mechanics and Engineering* 282 (2014) 132–160.
- [56] A. Ortiz-Bernardin, A. Russo, N. Sukumar, Consistent and stable meshfree Galerkin methods using the virtual element decomposition, *International Journal for Numerical Methods in Engineering* 112 (7) (2017) 655–684.
- [57] L. Beirão da Veiga, F. Brezzi, L. D. Marini, Virtual elements for linear elasticity problems, *SIAM Journal on Numerical Analysis* 51 (2) (2013) 794–812.
- [58] F. M. Andrade Pires, E. A. de Souza Neto, J. L. de la Cuesta Padilla, An assessment of the average nodal volume formulation for the analysis of nearly incompressible solids under finite strains, *Communications in Numerical Methods in Engineering* 20 (7) (2004) 569–583.
- [59] L. Mascotto, Ill-conditioning in the virtual element method: Stabilizations and bases, *Numerical Methods for Partial Differential Equations* 34 (4) (2018) 1258–1281.
- [60] H. C. Elman, D. J. Silvester, A. J. Wathen, *Finite Elements and Fast Iterative Solvers: with Applications in Incompressible Fluid Dynamics*, Oxford University Press, Inc, NY, 2006.
- [61] S. P. Timoshenko, J. N. Goodier, *Theory of Elasticity*, 3rd Edition, McGraw-Hill, NY, 1970.
- [62] S. Salinas, N. Hitschfeld-Kahler, A. Ortiz-Bernardin, H. Si, Polylla: Polygonal meshing algorithm based on

terminal-edge regions (2022). [doi:10.48550/ARXIV.2201.11925](https://doi.org/10.48550/ARXIV.2201.11925).